Edge channel transport in graphene nanoribbons

Lennart Bours

September 6, 2016

Contents

Introduction iii
- 0.1 Motivation iv
- 0.2 Thesis structure v

1 Theory 1
- 1.1 Graphene 1
  - Graphene lattice and band structure 2
  - Nanoribbons 3
- 1.2 Quantum Hall physics 4
  - The anomalous quantum Hall effect 6
  - Edge reconstruction 8
  - Confining potential 9
- 1.3 Landauer-Büttiker calculations 10
  - Quantum Hall transport 10
  - nn' junctions 12
  - nn'n junctions 15

2 Fabrication 18
- 2.1 Cleanroom techniques 18
  - Exfoliation 18
  - Chemical Vapour Deposition 20
  - Defining contacts 20
  - Evaporation and lift-off 21
  - Etching the ribbon 21
- 2.2 Device design 22
  - Single ribbon devices 22
  - A series of ribbons 24

3 Characterization 26
- 3.1 Set up 26
- 3.2 Methods 26
- 3.3 Multiple ribbons device 28
- 3.4 Hysteresis 31

4 Scanning Gate Microscopy **33**
4.1 Set-up 33
Atomic Force Microscopy 33
4.2 Scanning Gate Microscopy 35
Detecting backscattering 36
SGM measurements 39
4.3 Discussion 47

5 Conclusions **50**

Bibliography **52**

Acknowledgements **57**

Introduction

This master thesis represents my work at the NEST laboratory of Scuola Normale Supriore in Pisa. Here I worked on the fabrication of graphene nanoribbon field effect transistors, as well as the characterization of these devices by several means, most notably Scanning Gate Microscopy (SGM). SGM aims to unite the best of both worlds: it combines traditional Atomic Force Microscopy (AFM) with the electric field effect, typically achieved with *global* gating through the backgate or local but *static* gating through splitgates. By applying a voltage on the metallic AFM tip one can achieve not only *local* gating, but also control this gating with microscopic precision.

Graphene, the famous 2D material, was first exfoliated in 2004 [1] and quickly gained a tremendous amount of attention. Research activity focused on graphene exploded, and the number of articles published every year has grown exponentially up to 2014, see figure 1.

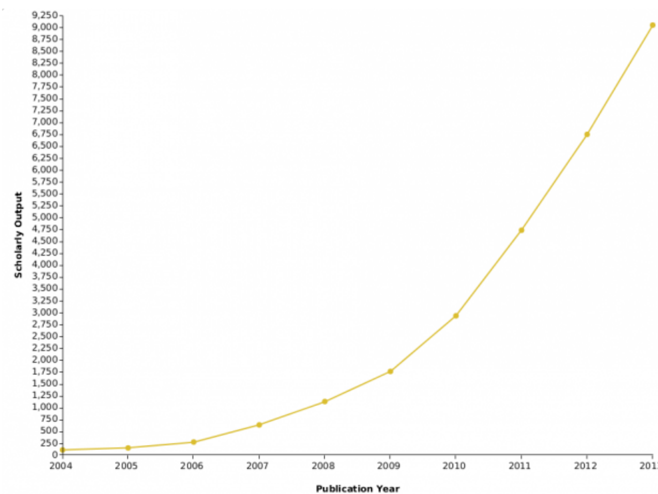

Figure 1: The number articles published in the period from 2004 to 2013 based on a search for 'graphene' in keywords, titles and abstracts. Source: SciVal.

The enormous amount of interest in graphene can be understood by its enormous potential. This first two-dimensional crystal showed many incredible properties and hence offers many new opportunities [2]. From high mobility electronic transport by massless Dirac fermions and many other anomalous effects, to record breaking mechanical strength, useful optical properties and more.

The Graphene Flagship Consortium[1] has, hoping to exploit graphene's remarkable properties, organized research lines in a wide range of topics. From fundamental research on graphene, other newly found 2D materials and composites of those to industrial production, high frequency and flexible electronics, spintronics, sensors, detectors and energy storage.

Conveniently, one can produce high quality material for research purposes with simple household scotch-tape.

0.1 Motivation

The Scanning Gate Microscope (SGM) set-up offers a local handle by which one can manipulate electronic transport. This opens up many interesting possibilities that are not granted in other experimental set-ups. On can, for example, study transport on a microscopic scale *inside* devices. With access to reasonably strong magnetic fields, one can study and manipulate transport in the quantum Hall regime. Using the SGM, one can determine the edge channel structure and determine if edge channel reconstruction takes place. This kind of work has been done on semiconductor 2DEGs [3, 4, 5], but not yet on graphene.

Graphene is alluring due to its inherent 2D nature, its relativistic properties and anomalous physics. Particularly interesting is the (inner) structure of the edge channels in the quantum Hall effect.

The chiral and robust nature of the quantum Hall effect offers and ideal laboratory for quantum transport experiments in one dimension. Notably, edge states of topologically ordered 2DEG systems are expected to display the so called 'edge-bulk' correspondence, which plays a pivotal role in quantum Hall based quantum computing [6, 7, 8]. Although the aim of QH based quantum computing is to exploit non-Abelian statistics of certain fractional Hall state quasi particles, it appears to be exceedingly difficult to realise these states in experiment [9, 10].

The occurrence of electronic reconstruction forms the most likely obstacle, since it destroys the 'topologically protected' state and hence the required edge-bulk correspondence. In short, a system that shows no electrostatic reconstruction is required. Since graphene naturally provides a 2DEG with

[1] A gigantic European project which started in 2013 and now well under way. Focused on graphene and its many aspects, its brings to the table a budget of one billion Euro.

an atomically sharp confining potential, it is a interesting candidate for this kind of physics.

Note that, although investigating the fractional quantum Hall effect was not attempted for this thesis, the structure of the integer Hall effect edge channels should reveal whether or not reconstruction takes place.

Throughout this thesis the term 'graphene nanoribbons' will be routinely used when describing or referring to our devices, because the experiment requires a thin and long device which thus resembles a ribbon. Note however, that the ribbons discussed in this thesis are typically around 800 nm wide and several μm long and are thus significantly larger then the (extremely) narrow ribbons which are expected to show for example, transversal quantization and a band gap. The ribbon shape is chosen because it is suitable for the SGM experiment, and should not modify transport in any way.

0.2 Thesis structure

This thesis consists of five chapters. Firstly a brief overview of graphene's deviant (and relevant) properties is given, together with a more in depth review of the quantum Hall physics which form the theoretical basis of this project. In the second chapter device fabrication is discussed. The following chapter, entitled Characterization, contains information about the properties and quality of several devices and magneto-transport measurements are presented. The fourth chapter presents the details and results of the SGM experiments and forms the core of this thesis. In the fifth and final chapter a conclusion of this work is given.

Chapter 1

Theory

The aim of the first section of this chapter is to briefly review some of the basic properties of graphene and effects that are relevant for understanding and characterizing graphene's behaviour. Unless otherwise specified the reader is referred to the review articles [11] and [12] for more information about specific topics. The theory of quantum Hall physics in graphene, which is central to this thesis, will be discussed in a separate section. The last section features the relevant Landauer-Büttiker calculations, which are crucial for understanding the results presented later.

1.1 Graphene

Graphene is an allotrope of carbon that appears as one single layer of carbon atoms arranged in a hexagonal or 'honeycomb' lattice. This two dimensional crystal has been studied since 1947 [13] because of its relation to graphite, carbon nanotubes, fullerenes, the interesting properties of this family and its theoretical accessibility. For a long time this was considered a purely hypothetical exercise, as the Mermin-Wagner theorem predicts that (free standing) 2D crystals are unstable at any finite temperature, due to the logarithmic divergence in the out of plane acoustic phonons as $\vec{q} \to 0$ [14].

Nevertheless, Geim and Novoselov succeeded in isolating graphene in 2004 [1] and hereby opened up a field that would expand rapidly. Graphene immediately attracted much attention due to its perplexing mechanical and electronic properties. In 2010 Geim and Novosolov where awarded the Nobel prize in physics

> "for ground breaking experiments regarding the two-dimensional material graphene."

Graphene lattice and band structure

In graphene the carbon atoms are bound to each other by the sp^2 hybridization of the atomic orbitals s, p_x and p_y. The distance separating two neighbouring lattice sites is $a = |\delta| = 1.42$ Å (figure 1.1a). The hexagonal lattice can be constructed from two triangular Bravais lattices and thus has two carbon atoms per unit cell, generally referred to as sites A and B. As a consequence of this, the two carbon atoms at lattice sites A and B are distinct. The existence of these sublattices, combined with the symmetry properties of the crystal leads to some special properties, such as the valley degeneracy and the linear energy spectrum.

Graphene's basic lattice vectors $\vec{a}$ and reciprocal lattice vectors $\vec{b}$ are:

$$\vec{a_1} = \frac{a}{2}(3, \sqrt{3}) \qquad \vec{b_1} = \frac{2\pi}{3a}(1, \sqrt{3}) \tag{1.1}$$

$$\vec{a_2} = \frac{a}{2}(3, -\sqrt{3}) \qquad \vec{b_2} = \frac{2\pi}{3a}(1, -\sqrt{3}) \tag{1.2}$$

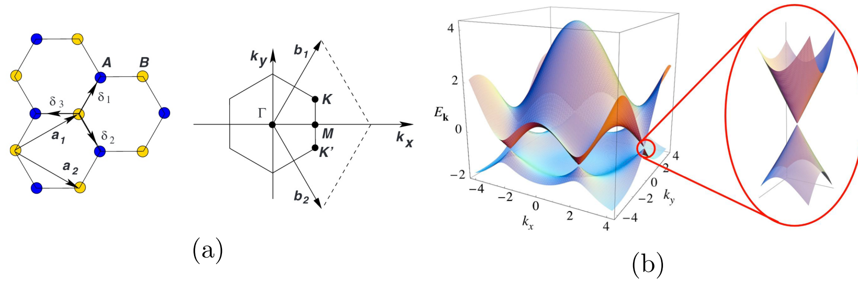

Figure 1.1: a) Graphene's hexagonal lattice with sublattices A and B and the Dirac points K and K' in the momentum space. b) The band structure of graphene calculated with the nearest neighbour approximation.

The reciprocal space of graphene is again hexagonal in shape, like the lattice itself. There are two special points in k-space, known as K and K'. These two 'Dirac points' (K and K') are especially important for electronic transport in graphene. In undoped graphene, the Fermi energy crosses the bands at these points, and for small deviations from this energy, the dispersion relation is linear (see figure 1.1b). In combination with the valley degeneracy, this gives rise to graphene's 'relativistic' transport properties. The position of the Dirac points is given by:

$$\vec{K} = (\frac{2\pi}{3a}, \frac{2\pi}{3\sqrt{3}a}) \qquad \vec{K}' = (\frac{2\pi}{3a}, -\frac{2\pi}{3\sqrt{3}a}) \tag{1.3}$$

Graphene's band structure can be calculated using the tight binding approximation, in which a Hamiltonian is constructed using the electrons'

hopping energies to nearby atoms. Solving this Hamiltonian for both nearest neighbour and next nearest neighbour hopping one finds the dispersion relation:

$$E_{\pm}(\vec{k}) = \pm t\sqrt{3 + f(\vec{k})} - t' f(\vec{k}) \tag{1.4}$$

with

$$f(\vec{k}) = 2\cos(\sqrt{3}k_y a) + 4\cos(\frac{\sqrt{3}}{2}k_y a)\cos(\frac{3}{2}k_x a) \tag{1.5}$$

The plus and minus signs denote the conduction and the valance band, respectively. The nearest neighbour and next nearest neighbour electron hopping energies are respectively $t \approx 2.8$ eV, and t' is estimated between $0.02 \cdot t$ and $0.2 \cdot t$. The conduction band and valance band touch at the K and K' points, in undoped graphene the Fermi energy crosses the energy bands here.

The next nearest neighbour hopping parameter t' breaks the symmetry between the conductance and valance band. Like other higher order perturbations that warp or shift graphene's band structure, the effects of t' can be neglected for energies close to 0, where the dispersion relation (equation (1.4)) is approximated to be linear by expanding it close to the Dirac points. With $\vec{k} = \vec{K} + \vec{q}$ and $|\vec{q}| \ll |\vec{K}|$ the band structure takes the 'relativistic' form:

$$E_{\pm}(\vec{q}) \approx \pm v_F|\vec{q}| \tag{1.6}$$

where $v_F = \frac{3ta}{2} \approx 10^6$ m/s.

Thus, for low energies, the charge carrier energy is proportional to its momentum and the Fermi velocity v_F, which is constant and roughly 300 times smaller than c. A picture of the band structure close to the Fermi energy is shown in figure 1.1b on the preceding page, with a close up of the linear dispersion relation close to the Dirac points.

Nanoribbons

After the isolation of graphene became routine, an interest into graphene nanoribbons quickly developed. These promise control over the electronic properties of the graphene —most notably the band gap— if one succeeds in fabricating ribbons so narrow that lateral confinement of the electrons becomes important. In order to engineer the band gap, an enormous control is required. In theory the state of the ribbon can change between conducting and insulating by adding a single row of carbon atoms to the ribbons width.

Furthermore, the ribbon's edge structure, so called 'zig-zag' or 'armchair', also affects transport and can lead to special 'edge states'[1].

Several groups have attempted to open a band gap using lateral confinement. As early as 2007 a suppression of the minimal conductance at low charge carrier densities was reported for ribbons with a width smaller than 100 nm [15]. A later work reported that this suppression in narrow ribbons with a width of 60 nm was not due to lateral confinement but rather due to charge related effects which created quantum dots in the narrow devices [16].

The width of the nanoribbons fabricated for this thesis ranged from 200 nm to 800 nm, with ribbons of the latter dimension used for SGM experiments. The devices are therefore much larger than the widths which are typically required to see a suppression of the minimum conductance in experiments.

1.2 Quantum Hall physics

In 1980 von Klitzing discovered that the quantum Hall effect was precisely quantized, a feat for which he was awarded the Nobel prize in physics a mere 5 years later. A theoretical explanation for the the quantized Hall conductivity was first given by Laughlin [17], who used a gauge invariance argument to derive the exact result. Halperin later extended this work by describing the particular 'extended (edge) states' and showed how a moderate amount of disorder does not disturb the exact quantization of conductance.

When confined into two dimensions and subjected to an external magnetic field perpendicular to this plane, electrons follow closed circular paths known as cyclotron orbits. The electron states condense into a spectrum of Landau levels which are equidistant in energy and macroscopically degenerate. Using the electron charge e, the magnetic field B and cyclotron mass m, we can derive the cyclotron frequency

$$\omega_c = eB/m \tag{1.7}$$

which is convenient for expressing the electron energy spectrum in two-dimensional systems:

$$E_n = \hbar\omega_c(n + \frac{1}{2}) \tag{1.8}$$

In the 2D case, the degeneracy of these levels is likewise dependent on the external magnetic field:

$$N = \frac{BA}{\phi_0} \tag{1.9}$$

[1]Note that these edge states are a consequence of the edge geometry and appear in zero magnetic field. They are wholly unrelated to the quantum Hall effect and throughout this thesis 'edge states' is generally used to refer to the quantum Hall variety.

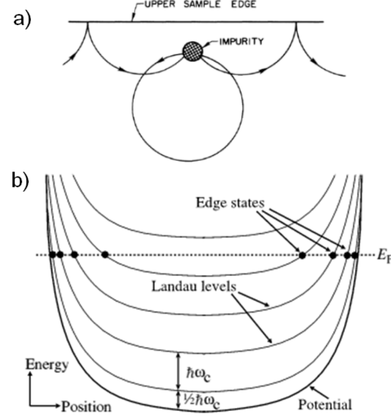

Figure 1.2: a) In a magnetic field, time reversal symmetry is broken and hence, backscattering is suppressed. b) Landau levels in the classical quantum Hall effect. The horizontal axis represent the width of the 2D system. The thick line represents the confining potential which bends the levels upwards close to the edges, where they will inevitability cross the Fermi level.

with sample area A and the flux quantum $\phi_0 = h/2e$. Note that the Landau levels can be further degenerate due to spin (assuming the Zeeman splitting negligible) or valley degeneracy.

The quantization of the cyclotron orbit and subsequent formation of Landau levels leads to macroscopically accessible quantum effects such as the Shubnikov-de Haas oscillations and the de Haas-van Alphen effect, which are oscillations in the longitudinal conductivity and magnetic moment, respectively.

If the splitting between the Landau levels $\Delta E = \hbar\omega_c$ becomes larger than the broadening of the levels, gaps appear in the density of states. When the Fermi energy lies in between two well separated levels, electrons located in the bulk of the system become localized, while electron states at the edge are de-localized (often portrayed semi-classically as 'skipping orbits').

The number of edge channels is given by the number of Landau levels with an energy lower than E_F, i.e. the filling factor ν. The energy of these levels is lower than the Fermi energy in the bulk of the system, but the levels are pushed upwards by a confining potential that defines the edges of the 2DEG (figure 1.2). The position where the Landau levels cross the Fermi energy denotes the position of the edge channel. If the Landau levels are spin degenerate (ignoring the Zeeman splitting), the sequence of filling factors in the integer quantum Hall effect is

$$\nu = g_s g_v n \tag{1.10}$$

with n the number of filled Landau levels, g_s the spin degeneracy and g_v valley degeneracy.

The edge channels are chiral, and electrons on opposite sides of the system move in opposite directions. If the sample edges are spatially well separated and the disorder is not too large, scattering from one edge to the other is impossible and hence backscattering is strongly suppressed [18]. The edge

channels along one side of the sample are necessarily in equilibrium and the longitudinal resistance R_{xx} drops to zero.

If electrons are injected into the edge channels on one side of the sample and collected on the other, a non-zero Hall voltage can be measured, due to the difference in the chemical potential between the two opposing edges. The corresponding Hall resistance $R_{xy} = h/(\nu e^2)$ is quantized and appears as a plateau when the Fermi energy is between two well separated Landau levels. The resistance of this plateau depends on number of edge channels through which transport can occur, also known as the filling factor ν. When the Fermi energy crosses a Landau level, the Hall resistance smoothly and monotonically increases to the next plateau.

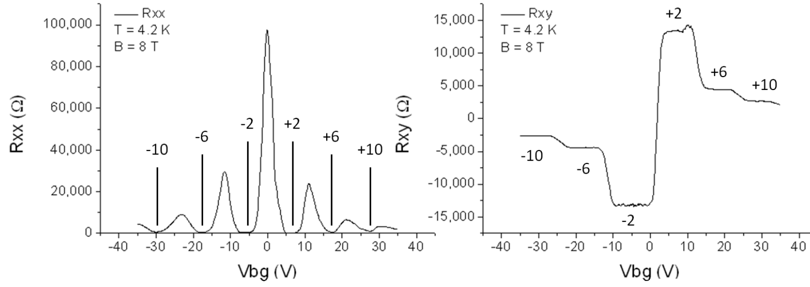

Figure 1.3: The quantum Hall effect as seen in device G2, while sweeping the backgate in a magnetic field of 8 T at 4.2 K. The filling factors $\pm 2, \pm 6$ and ± 10 are well defined and clearly visible.

The anomalous quantum Hall effect

Figure 1.3 shows the anomalous quantum Hall effect as seen in our devices. Note that, for clarity, the Hall resistance and filling factors will be assigned a negative value on the hole side throughout this thesis.

The quantum Hall effect and other relevant physics have to be slightly modified when applied to graphene, due to its particular band structure and symmetry. The cyclotron mass, for example, is now dependent on the electron density, as a direct consequence of the massless Dirac-like dispersion.

$$m^* = \frac{\sqrt{\pi}}{v_F}\sqrt{n} \tag{1.11}$$

The cyclotron frequency can be expressed using the magnetic length $l_B = \sqrt{c/eB}$ which leads to the modified expression:

$$\omega_c = \sqrt{2}\frac{v_F}{l_B} \tag{1.12}$$

and hence the cyclotron energy scales with $\sqrt{B}$ as opposed to scaling with B in classical Hall physics (equation (1.7) on page 4). This discrepancy in

scaling leads to energy spectra which are rather different than the ones found in ordinary 2DEGs. For example, at fields $B \approx 10$ T the 2DEG cyclotron energy is of the order of 10 K, whereas the Direac fermion cyclotron energy is around 1000 K. The large cyclotron energy means that the quantum Hall effect in graphene can be observed even at room temperature [19]. Furthermore, at $B = 10$ T the Zeeman energy $g\mu_B B \approx 5$ K is small compared to the cyclotron energy, and can be neglected in graphene.

The most important consequence of the unique nature of charge carriers in graphene is that the Landau levels are no longer spaced equidistantly, but follow a square root dependency:

$$E = \pm\sqrt{\frac{2eB\hbar v_F^2}{c}(n + \frac{1}{2} \pm \frac{1}{2})} \tag{1.13}$$

or

$$E_\pm(n) = \pm\hbar\omega_c\sqrt{n} \tag{1.14}$$

where $n = 0, 1, 2\ldots$ is a positive integer. Note that the Landau level degeneracy in the 2D bulk is identical to the one from the general case equation (1.9) on page 4.

The Landau levels at the two Dirac points K and K' have the exact same energy spectrum and hence every level is fourfold degenerate (two times for spin and two times for valley). The important exception is the anomalous zero energy Landau level, which is shared by electrons and holes and only contributes 2 modes to transport in either the hole or the electron regime, instead of the 4 modes contributed by all other levels. This gives the modified sequence of filling factors

$$\nu = \pm g_s g_v\left(n + \frac{1}{2}\right) \tag{1.15}$$

with $n = 0, 1, 2\ldots$, $g_s = 2$ the spin degeneracy and $g_v = 2$ the valley degeneracy in graphene. Due to the extra $\frac{1}{2}$ term compared with equation (1.10) on page 5, the anomalous quantum Hall effect in graphene is also called the half-integer quantum Hall effect.

The appearance of the zero energy Landau level is due to the absence of the normal $+1/2$ term in equation (1.14). When solving the system's relativistic Hamiltonian it vanishes because of the exact cancellation of the cyclotron energy and a pseudo Zeeman term[2] (the second and last terms in equation (1.13), respectively) which represents the electrons 'orbital motion'; the hopping process between neighbouring lattice sites.

The special nature of the zero energy level is a consequence of the Atiya-Singer index theorem, which tells us that this energy level is topologically

[2]A similar situation occurs in free electrons, where the cyclotron mass is equal to the effective mass and both terms also cancel each other out. In semiconductors the cyclotron mass is usually much smaller and the Zeeman term becomes a small correction.

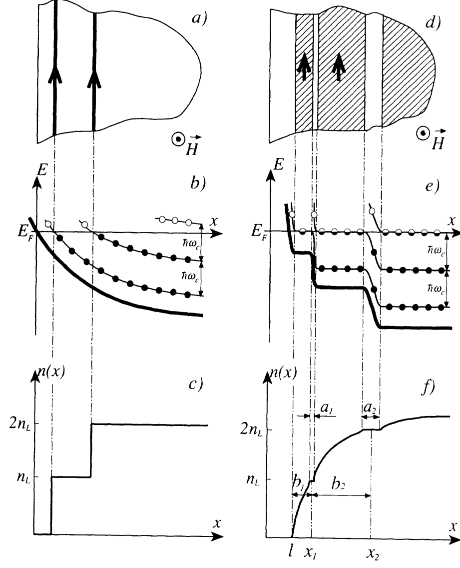

Figure 1.4: a) A top view of the 2DEG system with the arrows illustrating electron flow. b) The confining potential adiabatically bends the Landau levels upwards close to the edge. Full dots denote filled states, empty dots denote empty states. c) The corresponding electron density as a function of the distance from the sample edge. d) After reconstruction: the shaded regions are compressible strips with a non-integer filling factor, the unshaded strips have integer filling factors and are incompressible. e) The electrostatic potential and Landau levels. Half filled dots indicate partially occupied levels. f) The electron density as a function of the distance from the edge. From [21].

protected against inhomogeneities in the magnetic field, since it is only dependent on the *total* flux. This is particularly relevant since the level is robust with respect to the inhomogeneitis created by ripples and is protected against broadening which can be discerned experimentally [20].

In summary, the quantum Hall effect in graphene differs from the normal quantum Hall effect, most importantly in the square root dependence of the Landau levels on the charge density and the absence of a constant energy term $\frac{1}{2}\hbar\omega_C$. Every level is fourfold degenerate, except for the zero energy level which is divided between electrons and holes and therefore only contributes 2 modes to transport. Furthermore, the zero energy level is topologically protected against broadening due to an inhomogeneous magnetic field.

Edge reconstruction

The naive picture drawn by Halperin leads to discrete jumps in the electron density when the Landau levels cross the Fermi energy, see figure 1.4. This in turn would lead to large electrostatic forces and seems an unrealistic picture.

This issue was addressed by proposing a many body 'electrostatic reconstruction' of the edge states which relaxes the electrostatic potential [21, 22]. If the confining potential is smooth (parabolic), then the electrons can gain energy by locally redistributing themselves and thus screening out the discrete jumps in charge. Subsequently every edge channel splits into a compressible and an incompressible strip. The width of these strips depends

on the filling factor and the steepness of the confining potential. Furthermore, they scale with the width of the 2DEG. A smooth confinement potential is typical for semiconductor 2DEG systems where the boundaries often are created by electrostatic potentials supplied by gates. And even if a sharp edge is created through etching, surface band banding due to Fermi level pinning at the edge of the sample still tends to smoothen out the confining potential.

The electron wave function overlap of electrons belonging to different edge states is exponentially small, such that the different edge states are effectively isolated in the absence of disorder, although in experiment the minimum length required before parallel channels equilibrate is usually comparable or smaller than the sample size; of the order of microns [23]. Depending on the filling factor, there can be either a compressible or an incompressible state in the centre of the system. These configurations are referred to as the 'C-state' and 'I-state' respectively.

Confining potential

The electrostatic reconstruction hinges on the assumption that the confining potential is sufficiently smooth, such that it allows the redistribution of the electrons. It has been suggested that if the edge potential is very sharp, reconstruction cannot take place [24] and edge-bulk correspondence is maintained (see section 0.1 on page iv). In this regard, graphene seems a promising system as its confining potential is sharp on an atomic length scale.

However, there is a second important argument that considers screening of the gate potential. Typical devices are fabricated on Si/SiO_2 wafers, where the highly doped, metallic Si is used as a backgate and a 300 nm thick SiO_2 top layer insulates the device from the backgate. By applying a voltage to the back gate, a considerable amount of charge is induced in the graphene. The electric field generated by these charges induces image charges 0.3 µm below the Si surface, which screen out this electric field at the Si surface.

The large distance[3] (0.6 µm) between these image charges and the device tends to induce a macroscopic charge accumulation along the boundaries of thin, µm sized graphene strips [25].

This charge accumulation along the edges of the graphene leads to a smoothing of the confining potential, as depicted in figure 1.5 on the following page; the potential is zero inside the sample —if the dimensions of the sample are larger than the distance between the sample and the backgate— but tends to non-zero values at the boundary of the device. If the potential

[3] In the quantum Hall regime the distance between the backgate and the device should be compared to the magnetic length $l_B \approx 26\ \text{nm}/\sqrt{B}$ where B is the magnetic field in Tesla.

becomes sufficiently smooth, electronic reconstruction of the edge channels becomes possible again.

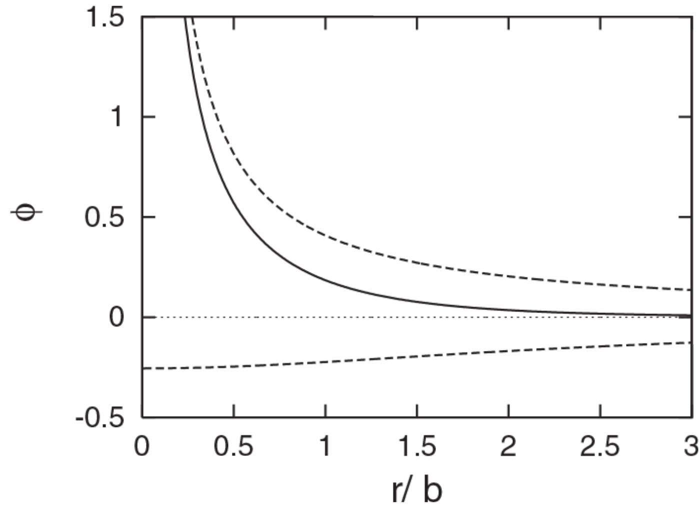

Figure 1.5: The screening of an electric potential ϕ at the surface of a 300 nm thick insulator with $\epsilon = 3.9$ (SiO_2). The screened potential is shown by the solid line, the upper dashed line shows the potential of the surface charge without image charges in the backgate (induced by the charge of the device). The lower dashed line represents the difference between the two. The in-plane distance $r = \sqrt{x^2 + y^2}$ in measured in units of the insulating layer thickness, $b = 0.3$ µm. From [25].

1.3 Landauer-Büttiker calculations

This section features an overview of the relevant Landauer-Büttiker calculations [18] which will be needed to understand the SGM results later presented.

Quantum Hall transport

We describe transport at the microscopic level by attributing a current to all available electron states that contribute to transport. The series of delocalized states, that form a continues path, are known as channels. The edge states in the quantum Hall system can carry a current along the edges since the electron velocity $v \propto dE/dk$, which is non-zero only close to sample edge, where the Landau levels are bended upwards. Transport through a small number of (edge) channels can be conveniently described with the

Landauer-Büttiker formalism. If no backscattering takes place, every channel contributes exactly one unit of conductance

$$\sigma_0 = \frac{e^2}{h} \tag{1.16}$$

If scattering is possible, this value can become smaller. To determine the total conductance, one can simply sum all the contributions, taking into account the possibility of backscattering. Given a certain conductance, a current will flow if there is an imbalance in the chemical potential μ, which represents the energy of the electrons. By applying a voltage bias to one side of a device, we inject electrons with a chemical potential $\mu_1 > 0$ into the device, through a contact which is called the source contact. On the other side of the the device, a contact is grounded an thus has a chemical potential which we will define $\mu_2 \equiv 0$. Given the total conductance and a difference in the chemical potential $\Delta\mu = \mu_1 - \mu_2$, a current will flow

$$I = \frac{e}{h} \sum_{i,j=1}^{i,j=N} T_{ij} \Delta\mu \tag{1.17}$$

where $T_{ij} = |t_{ij}|^2$ is the transmission probability from channel i to channel j and we have assumed that the energy dependence of T_{ij} can be neglected in the (small) energy range between μ_1 and μ_2. The sum is to be taken over all channels to calculate the total transmitted current.

Using the voltage drop $eV = \Delta\mu$ we can find the Landauer resistance

$$R = \frac{h}{e^2} \frac{1}{T} \tag{1.18}$$

In the ideal case that all channels are transmitted perfectly (no scattering), the transmission probability becomes 1: $T = \sum_{i,j=1}^{i.j=N} T_{ij} = 1$ and thus the resistance becomes

$$R = \frac{h}{e^2} \frac{1}{N} \tag{1.19}$$

with N the number of channels.

We will now apply this formalism to the quantum Hall edge channels (section 1.2 on page 4). If we are in a region where the filling factor is an integer, R_{xx} drops to zero (backscattering is suppressed), while we see a plateau in R_{xy}. Since it is impossible to backscatter, the channels on one side of the sample must be at the same chemical potential. The contacts on the top of the sample are thus at the chemical potential of the source contact μ_s and the samples on the bottom are at a potential $\mu_d = 0$.

Due to the special nature of the zero energy Landau level in graphene (see section 1.2 on page 6), the first Landau level is two times degenerate, while all others are four times degenerate (two times for spin and two times

for valley degeneracy). The sequence of the number of channels contributing to transport is thus $N = 2, 6, 10\ldots$ (also known as the filling factor ν).

If the filling factor, and thus the number of edge channels, is known, it is straightforward to calculate the Hall resistance with equation (1.19) on the previous page, since

$$\frac{h}{e^2} \approx 25.8\ \mathrm{k}\Omega \tag{1.20}$$

thus

$$R_{xy} \approx 12.9\ \mathrm{k}\Omega \qquad \text{for } \nu = 2 \tag{1.21}$$

and

$$R_{xy} \approx 4.3\ \mathrm{k}\Omega \qquad \text{for } \nu = 6 \tag{1.22}$$

etc.

Thus, when the filling factor is integer, one will measure a longitudinal resistance $R_{xx} = 0$ and $R_{xy} \approx 25.8/\nu$ kΩ. See for example figure 1.6.

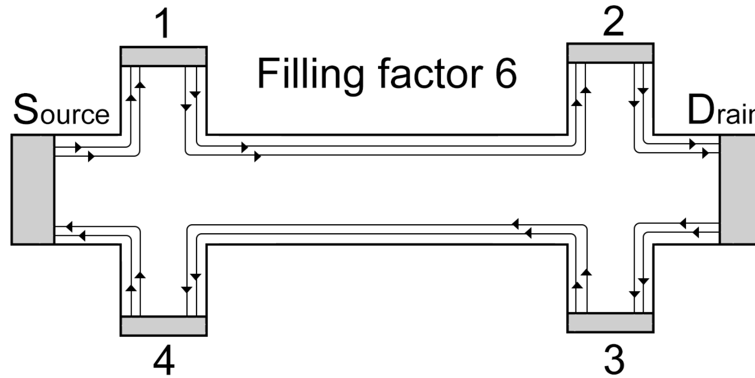

Figure 1.6: A schematic illustration of the quantum Hall effect in a Hall bar. The flow of electrons is denoted by the arrows. The outermost channel is twofold degenerate, while every other channel is fourfold degenerate, thus two filled Landau levels correspond to $\nu = 6$ edge channels, which corresponds to a Hall resistance of ≈ 4.3 kΩ.

nn' junctions

We assume ideal contacts which perfectly transmit all edge channels. The contact on the left is the current source and is at a chemical potential μ_s. The opposing contact on the right is the drain which we choose to be at $\mu_d = 0$. The other contacts are enumerated clockwise, in the top left is

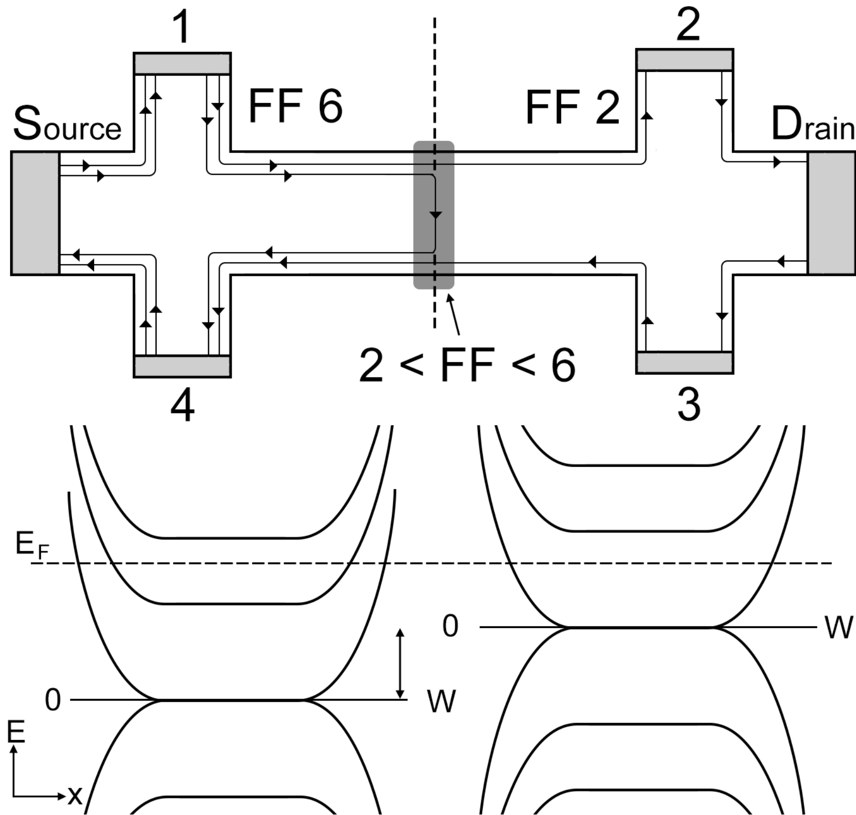

Figure 1.7: A schematic illustration of the quantum Hall effect in a Hall bar. A potential difference between the right and left side of the device is applied such that the right side of the device has a lower filling factor. It is thus inaccessible for the inner channels, whose Landau level has the highest energy. The channels are forced to backscatter from the top to the bottom of the device. In the bottom part of the figure, the position of the Fermi energy is shown with respect to the Landau levels for both regions. At the junction between the two regions there must be a non-integer filling factor between $\nu = 6$ and $\nu = 2$, where the second Landau level crosses the Fermi energy. In this region the bulk is conductive and hence current can flow (backscatter) from the top to the bottom edge of the device.

contact 1 and the bottom left is contact 4. In all examples presented in this chapter the current will flow through the sample in a clockwise manner, which corresponds to a magnetic field pointing upwards. If one would either change the charge carrier polarity or reverse the direction of the magnetic field, this flow would reverse, but the results stay the same.

We now discus a situation wherein the region on the left side of the sample (containing the contacts: source, 1 and 4) is at filling factor $\nu = 6$, while the right half, containing the other three contacts, is at filling factor $\nu = 2$, see figure 1.7 on the previous page. In this case the four channels corresponding to the second Landau level are backscattered before they reach the right side of the device.

To calculate the transmitted current we have to solve a set of equations (we already simplified by setting $\mu_d = 0$). Furthermore, we assume that the side probes do not transmit any current. This gives us the conditions $I_{1,2,3,4,} = 0$ and we chose $I_s = -I_d$. The number of channels on the right and left hand side is denoted by ν_r and ν_l respectively and $\nu_l > \nu_r$, then

$$\frac{h}{e}I = \nu_l \mu_s - (\nu_l - \nu_r)\mu_1 \tag{1.23}$$

$$0 = \nu_l \mu_1 - \nu_l \mu_s \tag{1.24}$$

$$0 = \nu_r \mu_2 - \nu_r \mu_1 \tag{1.25}$$

$$0 = \nu_r \mu_3 - 0 \tag{1.26}$$

$$0 = \nu_l \mu_4 - (\nu_l - \nu_r)\mu_1 \tag{1.27}$$

$\nu_l - \nu_r$ is the number of backscattered channels. It is straightforward to solve these equations

$$\mu_1 = \mu_s \rightarrow I = \frac{e}{h}\nu_r \mu_s \tag{1.28}$$

Thus, the current transmitted depends on the difference in chemical potential between the source and the drain $\Delta\mu = \mu_s - \mu_d = \mu_s$ and on the number of channels that flow from source to drain (in this case ν_r) at this chemical potential. The chemical potential of contact 3 is equal to μ_s, since the number of transmitted channels is ν_r and these are at μ_s. We can now calculate the measured Hall resistance on the right side of the device, between contacts 2 and 3, using the current derived in equation (1.28)

$$R_{23} = \frac{\Delta\mu}{eI} = \frac{h}{e^2}\frac{\mu_3 - \mu_2}{\nu_r \mu_s} = \frac{h}{e^2}\frac{(1-0)\mu_s}{\nu_r \mu_s} = \frac{h}{e^2}\frac{1}{\nu_r} \tag{1.29}$$

So, the Hall resistance between the two contacts on the right side of the device will reflect the filling factor in the right side of the device. For the contacts 1 and 4 on the left side of the device we plug in $\mu_1 = \mu_s$ and $\mu_4 = \frac{\nu_l - \nu_r}{\nu_l}\mu_s$

$$R_{14} = \frac{\Delta\mu}{eI} = \frac{h}{e^2}\frac{\left(\frac{\nu_l-\nu_r}{\nu_l}-1\right)\mu_s}{\nu_r\mu_s} = \frac{h}{e^2}\frac{1}{\nu_l} \tag{1.30}$$

So also the Hall contacts on the left side will detect the number of channels flowing in the left side. This result may seem counter intuitive at first, since the difference between the Hall contacts $\Delta\mu$ is no longer $\mu_s - \mu_d$, as it was when the filling factor was 2 in the whole device. The reason the measured resistance is unaffected when inducing the region with filling factor 1, is that the current has changed with $\Delta\mu$, from $I = \frac{e^2}{h}\nu_l\mu_s$ to $I = \frac{e^2}{h}\nu_r\mu_s$, cancelling out the change of $\Delta\mu$.

The source-drain resistance measures the lowest filling factor

$$R_{sd} = \frac{\Delta\mu}{eI} = \frac{h}{e^2}\frac{\mu_s}{\nu_r} \tag{1.31}$$

although, while measuring the source-drain resistance one would also be sensitive for the resistance of the contacts themselves, which might be significant.

Finally, also R_{xx} is unaffected;

$$R_{12} = \frac{\Delta\mu}{eI} = 0 \tag{1.32}$$

since contact 1 and contact 2 are both at the same chemical potential μ_s, even though the number of edge channels at these contacts is different. This holds for every combination of filling factors as long as both have the same sign, i.e. there is either an nn' or a pp' junction.

nn'n junctions

We will now discus $nn'n$ junctions. For example, first a global filling factor 6 is induced. Then, a region with filling factor 2 is induced in the centre of the device, see figure 1.8 on the next page.

This region does not extend to the contacts. Current is injected into the edge channels from the source, and flows along the top edge of the device. At the junction between the regions with filling factor 2 and 6, the bulk is conducting and the inner edge channels are backscattered from the top to the bottom of the device. The outer edge channels can flow through the device uninterrupted. Now $\nu_l = \nu_r \equiv \nu$ and the number of channels through the centre region is denoted $\nu' < \nu$, which gives us the following set of equations

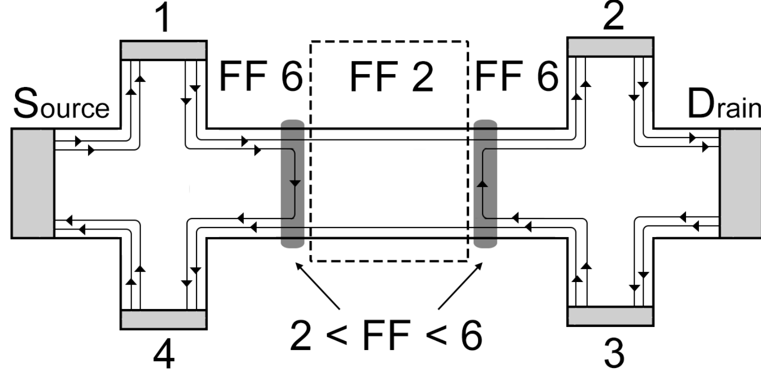

Figure 1.8: A schematic illustration of the quantum Hall effect in a Hall bar. The potential is now localized in the centre of the device, where it creates a region of filling factor $\nu = 2$, while the rest of the device is at filling factor $\nu = 6$.

$$\frac{h}{e}I = \nu\mu_s - (\nu - \nu')\mu_1 \tag{1.33}$$

$$0 = \nu\mu_1 - \nu\mu_s \tag{1.34}$$

$$0 = \nu\mu_2 - \nu'\mu_1 \tag{1.35}$$

$$0 = \nu\mu_3 - 0 \tag{1.36}$$

$$0 = \nu\mu_4 - (\nu - \nu')\mu_1 \tag{1.37}$$

This case is very similar to the one nn' junction, and again the Hall contacts are only sensitive to the number of channels at these contacts ν.

$$R_{xy} = \frac{h}{e^2}\frac{1}{\nu} \tag{1.38}$$

The difference is that R_{xx} is no longer zero

$$\mu_1 = \mu_s \rightarrow I = \frac{e^2}{h}\nu'\mu_s \tag{1.39}$$

$$R_{12} = \frac{\Delta\mu}{eI} = \frac{h}{e^2}\frac{\left(1 - \frac{\nu'}{\nu}\right)\mu_s}{\nu'\mu_s} = \frac{h}{e^2}\left(\frac{1}{\nu'} - \frac{1}{\nu}\right) \tag{1.40}$$

For $\nu = 6$ and $\nu' = 2$ this corresponds to:

$$R_{xx} = \frac{h}{e^2}\left(\frac{1}{2} - \frac{1}{6}\right) \approx 8.6\ \mathrm{k\Omega} \tag{1.41}$$

and for $\nu = 10$ and $\nu' = 6$

$$R_{xx} = \frac{h}{e^2}\left(\frac{1}{6} - \frac{1}{10}\right) \approx 1.7 \text{ k}\Omega \tag{1.42}$$

etc.

Thus, in the ideal case where the bulk of the sample is completely insulating (except of course at the nn' junction where the inner channels are backscattered) R_{xx} will be a non-zero value that illustrates the transport through the edge channels. In the ideal case this value will manifest as a plateau that imitates the well known plateaus of the Hall resistance R_{xy}.

It is also insightful to look at the diagonal contact configurations: $R_D^+ = R_{13}$ and $R_D^- = R_{24}$. We can calculate the expected resistance by simply adding or subtracting the resistances we already calculated: $R_D^{\pm} = R_{xy} \pm R_{xx}$, thus

$$R_D^+ = \frac{h}{e^2}\frac{1}{\nu'} \tag{1.43}$$

and

$$R_D^- = \frac{h}{e^2}\left(\frac{2}{\nu} - \frac{1}{\nu'}\right) \tag{1.44}$$

Thus, one can also determine the minimum filling factor in the central region by measuring the diagonal resistance R_D^+. The same is true for the source-drain resistance

$$R_{sd} = \frac{h}{e^2}\frac{1}{\nu'} \tag{1.45}$$

However, it should again be noted that, when using the source-drain resistance, one will have to subtract the contact resistances somehow.

A measurement of R_{xx} and R_{xy} thus provides the same information as a measurement of R_D^+ (or R_D^-, if one doesn't mind the inconvenience). To avoid redundancy, measurements of R_{xx} will be presented and discussed in this thesis.

Calculations similar to the ones presented above can be made for nn', where $\nu_n < \nu'_n$, np and npn junctions. In these cases the Hall resistance will take on fractional values as a consequence of the edge channels filled with electrons at the high chemical potential equilibrating with the 'empty' channels while flowing through the device [26, 27, 28]. Assuming the channels can fully equilibrate, this gives rise to fractional resistance values, which are unrelated to the fractional Hall effect. However, these are omitted here since they are not relevant for the work presented in this thesis.

Chapter 2

Fabrication

The first section of this chapter details which techniques were used to produce the devices for this work. In the second section the differences between several devices are discussed, and the motivation behind specific device designs is presented.

2.1 Cleanroom techniques

All devices measured were fabricated in the cleanroom of the NEST laboratory. Both exfoliated and graphene grown by Chemical Vapour Deposition (CVD) was used to fabricate graphene FETs.

Exfoliation

For exfoliated graphene, high quality graphite was deposited on a piece of scotch tape, and subsequently gently rubbed on a $\approx 1.5 \times 1.5\ \mathrm{cm}^2$ big Si/SiO_2 wafer covered with a layer of polyvinyl alcohol (PVA) and a 1 µm thick layer of poly-methyl methacrylate (PMMA).

The PMMA resides on top and is —like graphene— strongly hydrophobic and thus allows for the exfoliation of larger graphene flakes. The size and shape of the yielded graphene flakes can vary but is usually around several to several tens of micrometers long and wide. The graphene flakes are located with an optical microscope by their contrast [29] (figure 2.1a on the following page) and are then checked with Raman spectroscopy [30]. When a suitable flake is located, the wafer is placed in a Petri dish, and demi-water is slowly and carefully added. The water dissolves the PVA layer, so that the top PMMA layer (with the graphene on top) is detached from the Si wafer. The PMMA is strongly hydrophobic and thus starts to float on the water. If the procedure is performed successfully, the PMMA will float completely while the water will never have been in contact with the graphene.

The floating PMMA, with the target graphene flake on top, is then 'fished'

out of the water with a small, square, custom made piece of metal with an inner hole of ≈ 1 cm in diameter. The PMMA is positioned such that the target flake is located on the PMMA spanning the hole. The metal piece is then placed in a Karl Suss MJB4 mask aligner together with a custom made heater and a target chip. The chip is a clean piece of highly doped Si wafer with a 300 nm SiO_2 capping layer. It is $\approx 3 \times 3\,\text{mm}^2$ big and already has large conductive pads and a coordinate grid on top, created with UV-lithography and subsequent evaporation. These large chromium/gold pads will later be used to connect the electric wiring.

The target chip, which is placed on top of the heater, can be seen through the hole in the metal piece, since the PMMA is transparent. Thus, this configuration allows one to position the target graphene flake (which is attached to the bottom of the PMMA, facing the clean target chip) at a suitable location. When the alignment of the graphene flake and the target chip is satisfactory, the two are placed into contact and the heater is turned on. The heat softens the PMMA and improves the cohesion between the graphene flake and the SiO_2 substrate.

After a short time, the metal piece can be removed and the PMMA is now residing on top of the chip, with the graphene flake in between. The chip is then placed into acetone for several hours, which removes the PMMA. After the chip is taken out of the acetone, it is rinsed in isopropanol and dried with a nitrogen flow. The graphene flake is now located on a clean chip with a grid of markers and is ready to be processed.

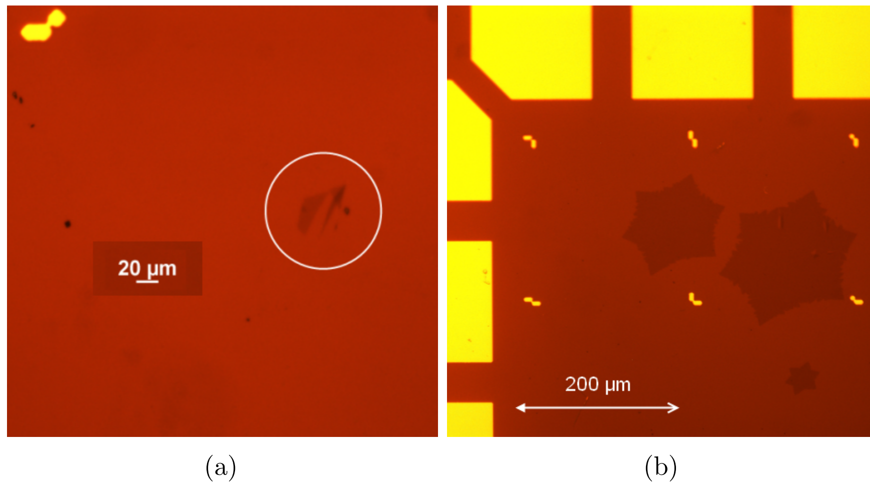

(a) (b)

Figure 2.1: a) Optical microscopy image of single layer graphene. b) Optical microscopy of single crystal monolayer graphene grown by CVD.

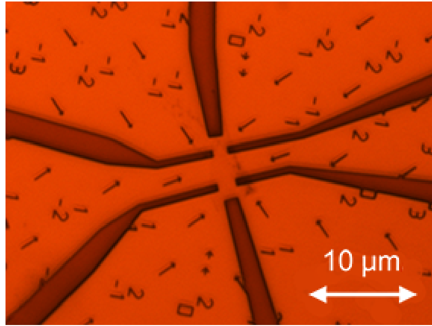

Figure 2.2:
Optical microscopy image showing the shape of contacts and SGM markers patterened in developed PMMA, before metallization. It is difficult to see the (exfoliated) graphene flake through the PMMA.

Chemical Vapour Deposition

In the case of CVD graphene, the procedure is similar. Large, single crystal, monolayer graphene flakes are grown at NEST on copper foil [31]. They are single crystals which can be up to several mm^2 long and wide (figure 2.1b on the previous page), and are of a quality comparable to exfoliated graphene on SiO_2 [32]. The samples are spin-coated with PMMA film, which is subsequently removed —together with the graphene— from the Cu substrate by electrochemical delamination [33]. The PMMA, carrying the graphene flakes, is then again collected with the metal piece, and the following procedure is identical to the one described in the section above.

Defining contacts

With the graphene on top of the chip a 300 nm thick layer of PMMA is spin-coated on top of the chip and the chip is baked at 120 °C for 15 minutes to crosslink the PMMA. Then, using a Zeiss Raith pattern generator and ELPHY multibeam plus Electron Beam Lithography software, the PMMA is exposed in a designed pattern using the pre existing UV makers as a reference for the position. In the areas where the PMMA is exposed to the electron beam, the high energy electrons deposit their energy and break the bonds holding the PMMA together, making it much easier to remove.

In this first lithography step, the ohmic contacts are patterned, connecting the graphene flake with the large, pre existing pads, which will later be used for bonding. In the same step, also a coordinate system of AFM markers is defined, which will be needed to find the device with atomic force microscopy. Finally, a set of Electron Beam Lithography markers are added to make sure that the second EBL patterning step will align nicely with the first.

After the exposure is complete, the sample is developed in AR 600-56 for two minutes. This removes the exposed PMMA, but leaves the PMMA in the areas which have not been exposed to the electron beam. The patterned features are checked with an optical microscope (figure 2.2), and the sample is then placed in a vacuum chamber where metal will be evaporated on the sample.

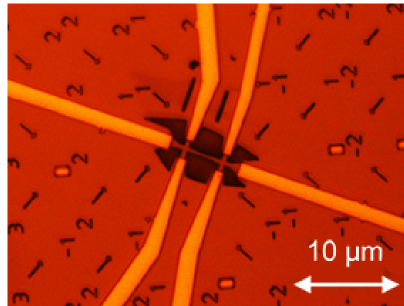

Figure 2.3:
Optical microscopy image taken before etching the ribbon. The graphene in the dark region will be removed by an oxygen plasma. The shape of the device is patterned using Electron Beam Lithography.

Evaporation and lift-off

The vacuum chamber of the evaporator is pumped until the pressure reaches $\approx 10^{-6}$ mbar. A thin layer of chromium is first thermally evaporated, followed by a layer of gold. The layers have a thickness of $\approx$ 5 nm and 50 nm, respectively. The metal will cover the whole sample surface, i.e. where there is PMMA, the metal will be on top of it, and where the PMMA was removed, the metal will be attached to the surface of the substrate.

The sample is then left in acetone for at least several hours, dissolving the PMMA. In the areas where the metal is unwanted, it is now no longer or barely supported. By flushing acetone over the sample with a syringe, the unwanted metal is washed away and only the patterned structures (the contacts, AFM markers and EBL markers) remain. After removing any PMMA leftovers with acetone, the sample is again rinsed with isopropanol and dried with a nitrogen flow.

Etching the ribbon

PMMA is again spin-coated on the sample and a second EBL step is performed. The EBL makers are used to precisely align the two exposures. This time, an area on top of and around the graphene flake is exposed. The exposure is then developed, as in the first EBL step. The graphene in the exposed areas will be removed in the next step, defining the desired shape of the device.

There is now PMMA covering the desired final device, i.e. the ribbon. There is still graphene around what will become the ribbon, but this is no longer protected by PMMA, see figure 2.3. The device is placed in a Reactive Ion Etching chamber, and using an oxygen plasma, the exposed graphene is etched away in 30 seconds. After removing the remaining PMMA, the device is finished.

None of the devices used where annealed after fabrication. In the final step, the chip with the complete device is glued to a chip carrier, using conductive silver paste to connect the backgate to the chip carrier. Using a wedge bonder, the large pads on the chip are connect to the pads of the chip carrier with a thin gold wire. The device can now be characterized by mounting the chip carrier in the experimental set-up.

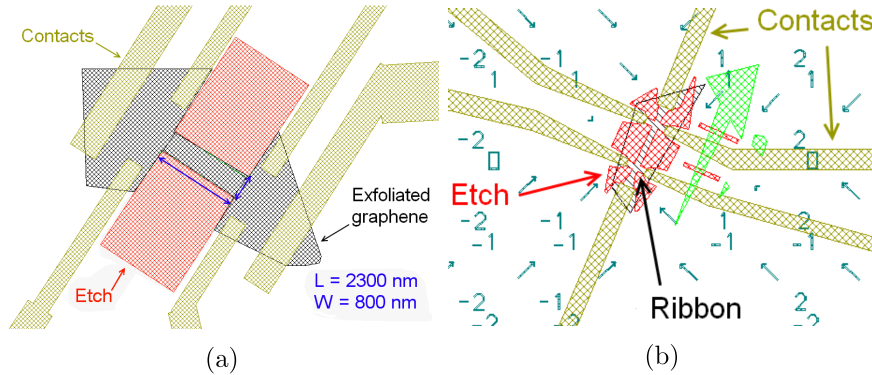

(a) (b)

Figure 2.4: a) Design for the first set of single ribbon devices. b) Design for the second set of single ribbon devices. The AFM marker grid is shown in dark green. Both ribbons are 800 nm wide.

2.2 Device design

The goal of this work is to investigate the backscattering of edge channels. For this to happen it must be possible to scatter these channels from one edge of the sample to the other, opposing edge (see also section 1.2 on page 4). This implies that the width of the device should not be larger than the 'spot size'[1] the SGM can induce.

Assuming the tip has the desired sharp and round shape, the effect of the tip will also be round. Since it is important that the effect of the tip is significant in only a section of the device, an elongated, narrow Hall bar like device or ribbon, is the obvious choice.

Although the ribbon cannot be too wide (compared to its length), there is also a danger of making it too narrow, for several reasons. It is theorized that when decreasing the width to below a hundred nanometre or so, transversal quantization becomes important; opening a band gap. When the width becomes very small, impurities can create quantum dot-like structures, strongly effecting transport. Finally, in extremely narrow devices, one enters a 1D regime in which the quantum Hall effect can behave very differently. See section 1.1 on page 3 for more information and references.

Single ribbon devices

The first set of nanoribbon devices were designed by S. Xiang, in a Hall bar-like configuration for four probe measurements (figure 2.4a). These devices had a width of between 0.8 and 1 µm and were several micrometers

[1]The spot size refers to the area in which the gating effect of the tip is significant. This depends on several factors, most importantly the voltage bias applied to the tip, and the distance between the tip and the device. See section 4.2 on page 39.

long[2]. All other devices used for this work, especially those used for the SGM studies, were designed and produced independently by the author.

When it later became clear that new devices would be necessary for SGM experiments, a second set was made with a slightly modified design (see figure 2.4b on the preceding page and figure 2.5). In order to reduce the invasiveness of the contacts [34], graphene leads were added to the design. This also has the advantage that the ribbon and therefore the geometrical factor is more clearly defined. Furthermore, the new design eliminated abrupt changes in the width of the graphene, which might affect transport due to mode-matching effects. These devices had a width of $W \approx 800$ nm and were 4 to 7 μm long.

The first set contained devices made from exfoliated graphene as well as devices made from CVD graphene. It was found that the quality of the exfoliated flakes was consistently higher than that of the CVD flakes. Since the extra large size of the CVD graphene flakes is not relevant for single ribbon devices, only samples fabricated from exfoliated graphene were used in the second set.

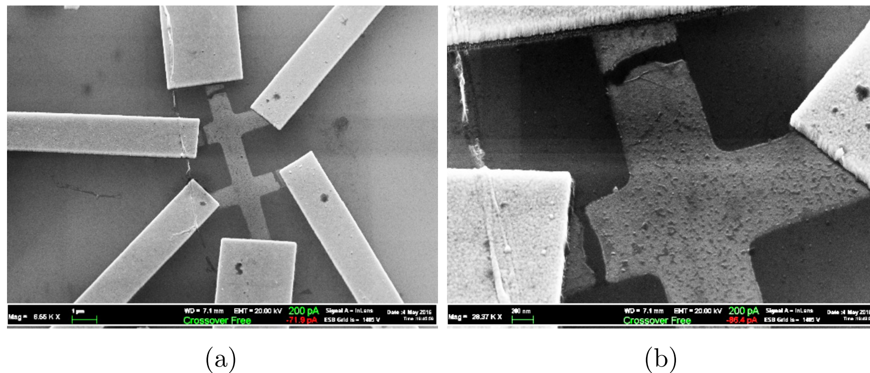

(a) (b)

Figure 2.5: a) and b) Two SEM pictures of a prototype device. The ribbon is 800 μm wide and roughly 2.5 nm long, making it relatively short. Note that the graphene —in this and in other devices— tends to break in the graphene 'leads', close to the contacts (although the same sometimes happens in the ribbon itself). These fractures were regularly noticed *after* the device had been used in an experiment. A possible explanation is the strain induced in the graphene during cooling and warming up the sample between ambient and liquid nitrogen/helium temperatures, due to the different thermal expansion coefficients of the graphene, the metal contacts and the substrate. Notably: for certain temperature regions the expansion coefficient of graphene is negative.

[2]The 'length' of the device/ribbon refers to the distance between the centres of the two longitudinal contacts throughout this thesis.

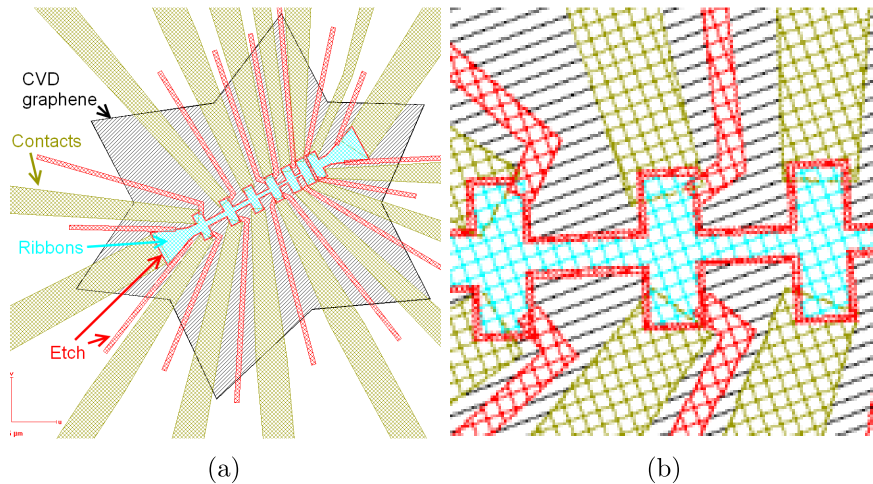

(a) (b)

Figure 2.6: a) The design of a device that consists of a series of six ribbons, which decrease in width from 600 to 100 nm. All ribbons have a length that is equal to four times their width. The device is fabricated using large, single crystal graphene flakes grown by CVD. The ribbons 'share' voltage probes. b) A zoom-in showing the two largest ribbons, which are 600 nm wide, 2.4 µm long and 500 nm wide, 2 µm long, respectively.

A series of ribbons

Besides the single ribbon devices which were studied with the Scanning Gate Microscope, a set of three identical devices, each of which featured a series of ribbons was produced (after the first set of single ribbon devices, but before the second). The purpose of these devices was to investigate the effect of the ribbon width on transport properties. These devices featured six ribbons in series, ranging in size from 100 to 600 nm, see figure 2.6 and figure 2.7 on the next page. Every ribbon within these devices has the same geometric factor $L/W = 4$ (the thinner ribbons are also shorter) so that it is straightforward to compare their resitivities.

These devices were made with CVD graphene flakes, since their large size allows one to place all six ribbons in one single device. This makes processing efficient and is convenient during the experiment, where one does not have to exchange and cool down many devices. Furthermore, since every device contains a set of ribbons, it is easy to make a fair comparison between the ribbons of different widths within one device, since they are made from one single crystal and their orientation with respect to the crystal lattice is identical.

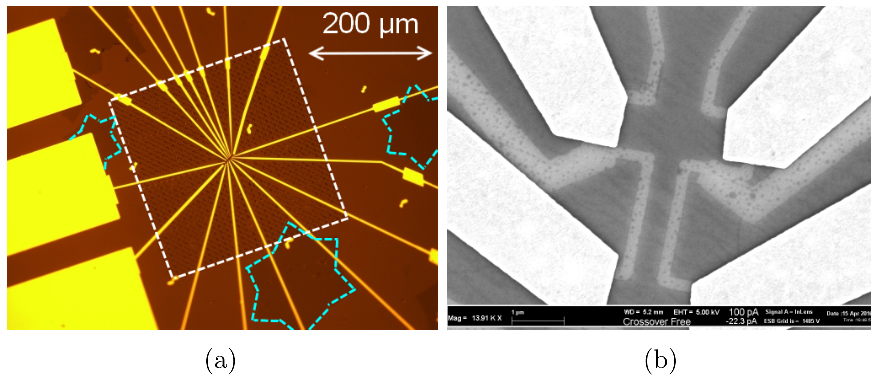

(a) (b)

Figure 2.7: a) A device with six nanoribbons seen through an optical microscope. The big gold pads on the left are used for bonding. The contacts are clearly visible and converge to the device, which is located at the centre of a square AFM marker grid (the white dashed line). Several other CVD crystals can be seen, as indicated by the light blue, dashed lines. b) A SEM micrograph that shows a close up of the 600 nm ribbon. The ohmic contacts appear white. Graphene covers the dark grey areas and the regions where graphene has been etched away are light grey. The nanoribbon is shown at the centre and is electrically isolated from the graphene at the sides. The source contact is connected at the top of this picture, where the central graphene strip diverges.

Chapter 3

Characterization

This chapter briefly discusses the set ups and methods used to test the samples before starting the SGM experiment. A separate section of this chapter is devoted to the devices which featured a series of six graphene ribbons. For information about the SGM set up and details regarding the SGM measurements see chapter 4 on page 33.

3.1 Set up

All measurements were performed using one or multiple lock-in amplifiers made by Stanford Research Systems (model SR830). Using the AC output, the source contact was biased with a large, 10 MΩ resistor in series, such that the current is effectively constant. To determine the device resistance we used four probe measurements in the standard Hall bar configuration, to avoid being sensitive to the contact resistances.

To modulate the backgate, a Keithley 2614B SourceMeter was used, and to bias the SGM tip we used a Yokogawa 7651 programmable DC source.

Preliminary characterization at room temperature was done using a 'dipstick', generally at a pressure of $\approx 10^{-4}$ mbar. The dipstick was also cooled down to liquid nitrogen and liquid helium temperatures.

3.2 Methods

Before moving the (single ribbon) devices to the Scanning Gate Microscope set-up, which is a complex and time consuming process, they where first characterized in less complicated set-ups. The main goal of these experiments was to confirm that the devices could exhibit a well defined quantum Hall effect, which is required for our SGM experiments.

The first step is to mount the device in a 'dipstick' which typically reaches a vacuum of $\approx 10^{-4}$ mbar. When the pressure is satisfactory, all contacts resistances are checked, and the longitudinal voltage drop V_{xx} is measured

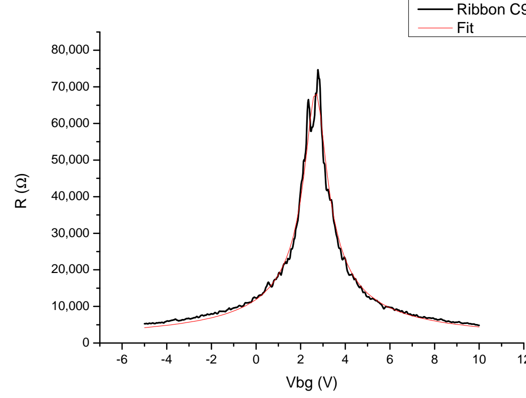

Figure 3.1: An example of a backgate sweep at $T = 300$ mK, including a fit with equation (3.4) on the following page. The estimated mobility and residual charge density from this fit: $\mu \approx 15.000$ cm/Vs^2 and $n_0 \approx 3.4 * 10^{10}$ cm^{-2}.

while sweeping the backgate. The position of maximum resistance, known as the Charge Neutrality Point (CNP or Dirac point), and the shape of this 'Dirac peak' offer the first hints of the device quality. Ideally, the position of the CNP should be at zero voltage on the backgate, $V_{bg} = 0$. This signifies that the graphene is not doped by unwanted defects, impurities or absorbates and thus the Fermi energy E_F coincides with the Dirac energy E_D. Realistically, a device with the CNP at $V_{cnp} \leq 10$ V on the backgate is considered good.

The resistivity ρ of the graphene is given by

$$\rho = \frac{W}{L} R, \tag{3.1}$$

with $R = V_{xx}/I_{SD}$ and L/W its geometrical factor (the length divided by the width). Since the magnetic field is zero, the conductivity is simply

$$\sigma = \frac{1}{\rho} = ne\mu, \tag{3.2}$$

where n is the electron (hole) density, e the electron (hole) charge $\approx \pm 1.6 * 10^{-19}$ C and μ the electron (hole) mobility.

The charge induced in the FET is estimated by treating the device as one plate of a parallel plate capacitor, and the backgate as the other. In this case the dielectric filling between the two plates is a 300 nm thick layer of SiO_2, with $\epsilon \approx 3.9$. Given the capacitance C the induced charge is

$$n = \frac{C}{e} |V_{bg} - V_{cnp}| = \frac{11.5}{1.6 * 10^{-19}} \frac{[\mu F/cm^2]}{[C]} = 7.2 * 10^{10} [V^{-1} cm^{-2}] * |V_{bg} - V_{cnp}| \tag{3.3}$$

Putting everything together, we find the following function, which is used to fit the backgate sweep in fitted in Origin:

$$R = \frac{L}{W}\left(e * \mu * \sqrt{n_0^2 + (7.2 * 10^{10} * (V_{bg} - V_{cnp}))^2}\right)^{-1} \tag{3.4}$$

n_0 is called the 'left over' or residual charge and represents the the charge inhomogeneity at the CNP.

From the fit the parameters μ and n_0 are extracted, giving an estimate of the sample quality (see figure 3.1 on the previous page). The procedure is repeated at low temperatures. For the samples measured in a magnetic field, electron density n and the Hall moblity μ can be estimated using the Hall effect and the Shubnikov-de Haas oscillations. The mobilities of the single ribbon devices, which were measured in the SGM varied between 8.000 and 14.000 cm^2/Vs.

The first set of single ribbon devices was characterized at temperatures down to 300 mK and in magnetic fields up to 10 T. The devices of the second set of single ribbon devices were only tested in the dipstick. Based the results of the equation (3.4) and previous experience, samples were selected and moved into the SGM. The devices typically showed nice quantum Hall traces, see figure 3.2 on the next page, figure 1.3 on page 6 and figure 3.3 on the next page. The quantum Hall plateaus are broad and well developed and R_{xy} increases monotonously. The longitudinal resistance R_{xx} shows clear Shubnikov-de Haas oscillations before becoming zero at $B = 3$ Tesla.

Besides the quantum Hall effect, also weak localization and universal conductance fluctuations were observed, but are not shown, nor discussed here.

3.3 Multiple ribbons device

Besides the single ribbon devices, also a set of devices with six ribbons, with widths between 100 and 600 nm, where characterized (see section 2.2 on page 24). All ribbons in these devices have the same geometrical factor $L/W = 4$, so their resistance ratios correspond to their resistivity ratios. In total three devices of this kind where produced, with the purpose of investigating the influence of ribbon width on transport properties.

Four probe measurements where performed at room temperature and at 4.2 Kelvin, see figure 3.4 on page 30 and figure 3.5 on page 30. The back gate sweeps were fitted with equation (3.4) to extract the electron mobility μ and residual charge n_0.

The resistivity of the ribbons increases with decreasing ribbon width. One possible explanation for this is that the disordered edge, which tends to localize states [35], becomes a relatively larger part of the ribbons as their width decreases. There is a striking increase in resistance between room temperature and 4.2 Kelvin, for the smallest ribbon. The high resistance close

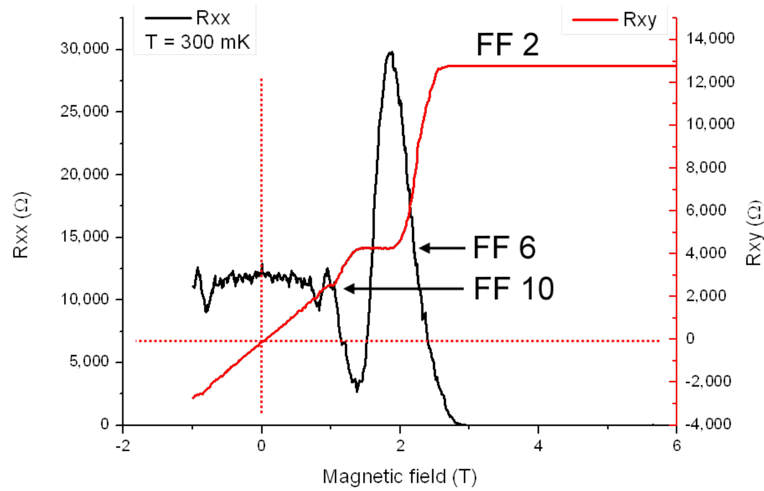

Figure 3.2: The quantum Hall effect as seen in device C9, while sweeping the magnetic field at 300 mK at $V_{bg} = 0$.

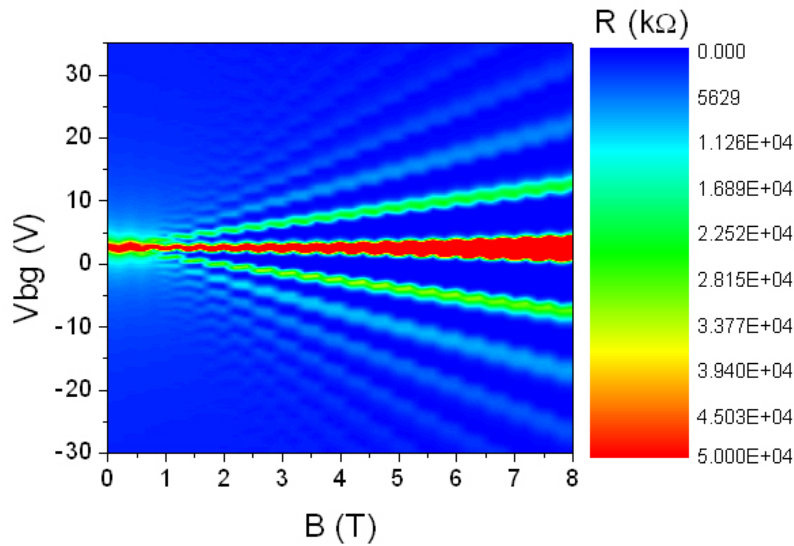

Figure 3.3: A Landau fan plot of the longitudinal resistance R_{xx}, while sweeping the backgate from -30 to +35 Volt and sweeping the magnetic field from 8 to 0 Tesla. Blue denotes a zero resistance, while red signifies a high resistance. ± 7 Landau levels are clearly visible.

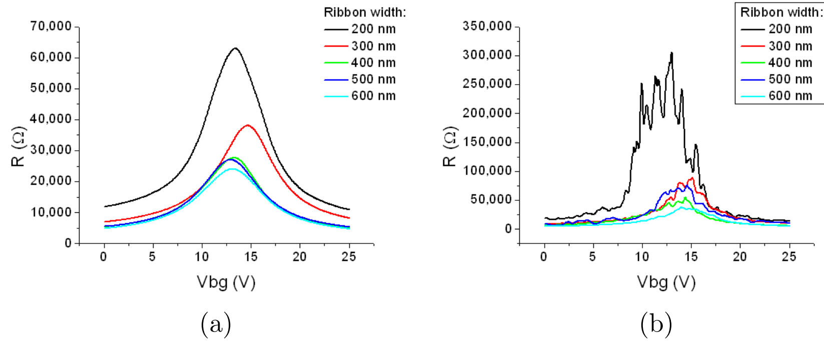

(a) (b)

Figure 3.4: a) The longitudinal resistances of five ribbons of one device (due to a bug in the EBL software, the 100 nm ribbon came out wrong). As all ribbons have the same geometrical factor, their R_{xx} plotted here is representative of their resistivity, which increases significantly for the thinner ribbons. b) The R_{xx} resistance of the same ribbons at 4.2 K. Universal conductance fluctuations are visible, and the resistance has increased dramatically for the thinner ribbons. The maximum resistance of the 200 nm ribbon has increased from 65 kΩ to 350 kΩ, while the maximum resistance of the 600 nm wide ribbon has changed from 25 kΩ to 37 kΩ.

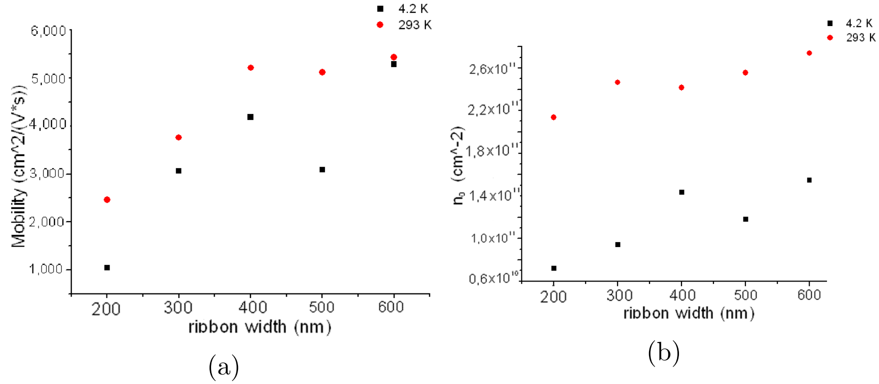

(a) (b)

Figure 3.5: Scatter plots of the mobility and of the residual charge density estimated through a fit of equation (3.4) on page 28. Both the mobility and the residual charge density decrease whith decreasing ribbon width.

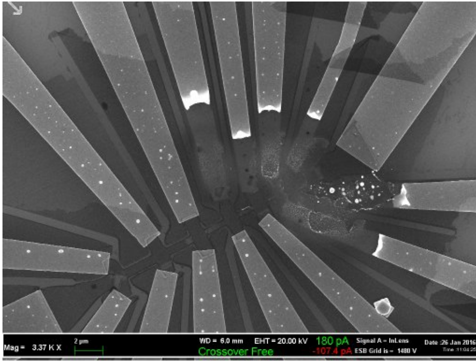

Figure 3.6: A post mortem scanning electron microscope image of one of the three devices that were produced with a series of six ribbons. A total of six contacts have been severely damaged, from what appears to be a catastrophic discharge of static electricity.

the the Charge Neutrality Point is due to the combined effect of a decrease in mobility μ from $2,500$ to $1,000$, and a decrease of n_0 from 2.2×10^{11} to 0.8×10^{11}. Thus the mobility and n_0 both decrease by a factor of ≈ 2.5. Since $R \cong \rho = 1/ne\mu$, this leads to an increase of R by a factor of ≈ 6.

Also notably are the large conductance fluctuations for this 200 nm wide ribbon at 4.2 K. These fluctuations were reproducible and were typically stable for several hours. This increase in both resistance and fluctuations could be due to an approach of the 1D regime, where coherent effects like conductance fluctuations can dominate the resistance [36, 37].

The original intention was to also characterize these devices in the quantum Hall regime. Unfortunately, the devices that looked promising both failed catastrophically before we were able to collect any data in a magnetic field (figure 3.6). A likely cause for this failure would be an electrostatic discharge, for which these devices could be extra sensitive due to their design.

Since it was clear that the mobility of the ribbons decreased with decreasing width and due to the lack of data in the quantum Hall regime —which is most important for the intended SGM experiments— it was decided to keep the width of the original devices. That is, the second set of single ribbon devices were, like the first, produced with a width of 800 nm, although their design was slightly modified.

3.4 Hysteresis

Several devices showed a particular, temperature dependent hysteresis. This effect was seen in most devices, but not in all. This hysteresis was completely absent at room temperature, but increases in magnitude at lower temperatures. Although we have only a small set of different temperatures available, the difference between 4.2 K and 300 mK is striking.

On one occasion, this hysteresis was monitored while the sample warmed up from 300 mK to 4.2 K. The magnitude of the hysteresis decreased greatly as the sample temperature approached 4.2 K.

This effect was not only seen across multiple devices, but also in different

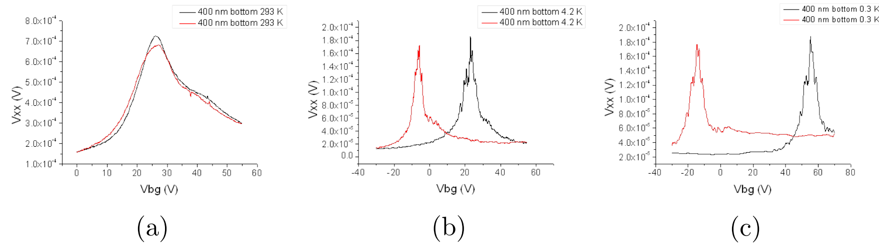

(a) (b) (c)

Figure 3.7: The temperature dependence of the hysteresis in a 400 nm wide ribbon. The black curves are taking sweeping the backgate from negative to positive voltages, and visa versa for the red curves. a) At room temperature there is no hysteresis. b) At 4.2 K, the distance between the two peaks is almost 30 V. c) At 300 mK, the magnitude of the hysteresis is 70 V.

set-ups, different cryostats and with different measuring equipment. Furthermore, using the same set-up, the hysteresis was observed in some devices, but not in others, even though the devices were prepared in nominally the same manner and around the same time. Thus is seems most likely that the hysteresis is not an artefact of measurement, but an intrinsic property of the devices.

The hysteresis appears to be very robust, as it decays very slowly, over the span of many hours. Furthermore, it is notable that the shape of the curve is not altered between many up and down sweeps. This suggest that, if we charge some parasitic capacitance, it must be far away from the device, such that its effect is homogeneous. Nevertheless, the cause of this particular hysteresis is not understood.

In order to account for this hysteresis, extra care was taken too make sure that different measurements are comparable. All the presented data was taken after first sweeping the backgate up and down at least once, such that the device was in a stable condition. Unless otherwise specified, all the curves shown are taken while sweeping the backgate from negative to positive voltages.

Chapter 4

Scanning Gate Microscopy

In this chapter, the measurements performed with our Scanning Gate Microscope are described, presented, and discussed. The first section gives a brief description of the SGM set-up. The second section explains the experimental procedures and the results. In the third and final section of this chapter, these results are interpreted and discussed.

4.1 Set-up

For the SGM measurements we used a modified commercial Attocube AFM system. Tungsten tips are prepared in our laboratory by chemical etching and subsequently glued to a tuning fork (figure 4.1a on the next page). The AFM operates in non-contact mode; the system detects the damping of the oscillation amplitude of the tuning fork that occurs when the tip is close to the sample surface, due to the shear force between the tip and the sample.

The microscope head contains a stack of piezo elements that allow for both course and fine movement, see figure 4.2 on the following page. The device sample holder is mounted opposite to the tip, and the whole system is thermally connected to the ^{3}He reservoir in the cold finger. The ^{3}He reservoir is itself adjacent to the 1K pot. By pumping on the ^{4}He in the 1K pot, the 1K pot reaches a temperature of 1.6 K, and the ^{3}He becomes liquid. When all the ^{3}He is liquefied, the ^{3}He reservoir is pumped with a charcoal pump. This way the cryostat reaches its base temperature of $\approx$ 300 mK. The entire cryostat is designed to be isolated from vibrations and noise. Note that for the sample discussed in this chapter, all measurements were performed at 4.2 K, to avoid a large hysteresis (see section 3.4 on page 31).

Atomic Force Microscopy

Initially, the ribbon is located through AFM, with the help of a coordinate grid that has been patterned around the device, together with the contacts.

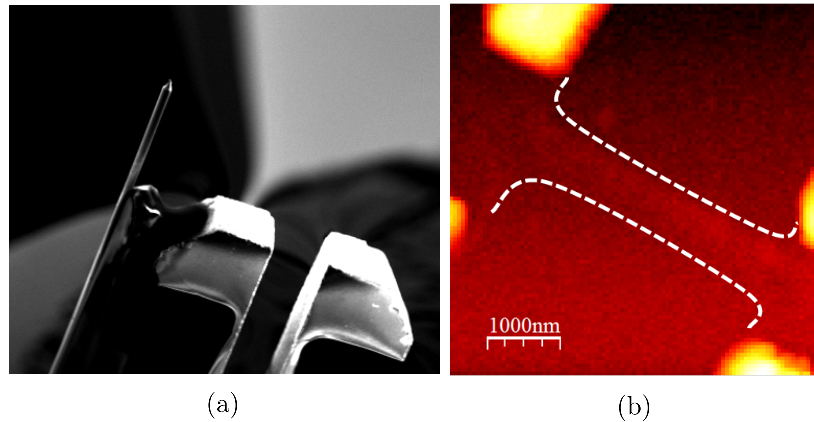

(a) (b)

Figure 4.1: a) SEM micrograph showing the tip, which is glued to one of the prongs of a tuning fork. b) False colour AFM image of the G4 nanoribbon, which has a width of 800 nm and is indicated by the dashed lines. The voltage probes, in Hall bar configuration are relatively high (50 – 80 nm) and appear yellow.

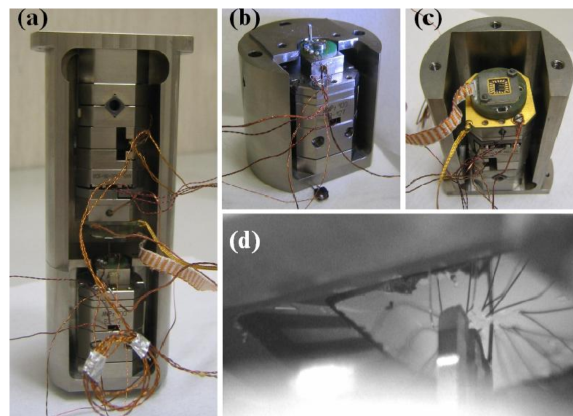

Figure 4.2: a) The microscope assembled. b) The lower part of the microscope consists of a titanium spacer, the piezo element for course movement in the z-direction, and the tip. c) The device, glued in a sample holder, is mounted on the top part of the microscope, on a stack of piezo elements for fine motion and for course motion in the x and y-direction. d) A close up of a device in the assembled microscope, showing the tuning fork and the microscope tip. Figure adapted from [5].

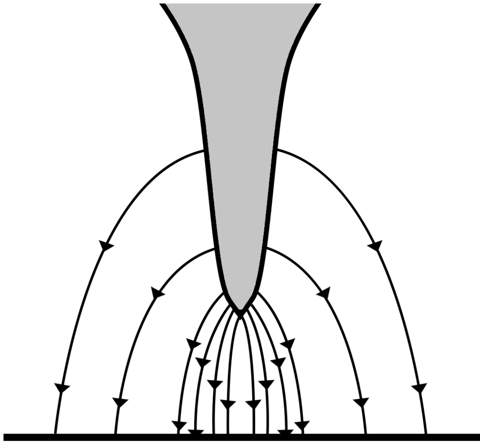

Figure 4.3: A schematic illustration of the electric field (and by extension the potential) that is generated applying a bias to the conductive tungsten tip. Electric charge accumulates at points where the surface of a conductor has a large curvature. A sharp tip therefore focuses the electric field in a small region underneath the tip. The generated potential is typically assumed to be Lorentzian in shape.

The high resolution of the microscope allowed us to see the graphene device in AFM (figure 4.1b on the preceding page). A reference AFM scan is taken every morning to adjust for a small overnight drift. This scan is then used to position the tip for the rest of the day.

4.2 Scanning Gate Microscopy

The goal of this work is to investigate the structure of quantum Hall edge channels in graphene by inducing backscattering of these channels with the SGM tip. The tip is made of tungsten, which has several desirable properties. Firstly and most importantly, it is conductive, and can therefore be used as a (scanning) gate by applying a voltage to the tip. Secondly, the hardness of the material makes it very suitable for AFM.

Because charge tends to accumulate at surfaces with a large curvature, the tip focusses the electric field, and thus the electrostatic potential, see figure 4.3. This potential is typically assumed to be Lorentzian in shape [38] and is particularly strong in the space directly beneath the sharp tip. The tip potential is somewhat screened by the charge carriers in the device, which tends to decrease the effective gating area, but can also create more complicated potential landscapes depending on the device geometry [39]. Since the graphene device is fabricated on top of the substrate, it is direly accessible with the tip and —avoiding the metal contacts— one can approach the device to ≈ 30 nm[1].

The AFM has typically a resolution between 1 and 10 nm, depending on the sharpness of the tip. This sharpness give a rough indication of the minimal area that can be gated by the tip, which is small compared to the

[1]In theory one can get as close with the tip as is desired, but you risk a catastrophic short between the graphene device and the conductive tip, which can be at 20 - 30 Volt. For the same reasons the (high) contacts have to be carefully avoided.

length and width of the nanoribbons (6 μm and 800 nm, respectively). The strength of the tip gating can be controlled by tuning the applied bias. A higher bias equals stronger gating, and also gating in a larger area. The area in which the tip gating is effective can also be tuned by changing the distance between the graphene ribbon and the tip. A larger (smaller) distance implies a weaker (stronger) effect in a larger (smaller) area. Thus, given the correct tuning of the tip distance and bias, the tip is expected to have a strong gating effect in an area which is small compared to the 6 μm long ribbon.

Note that throughout the following sections, 'small(er)' and 'large(r)' are used exclusively to refer to the *area* of the tip gating effect. When the *strength* of the electrostatic potential is discussed, the terms 'strong(er)' and 'weak(er)' are used.

To know the spot size (the effective gating area) of the tip is not a straightforward task. One can in principle calculate the expected potential shape and strength. However, to accurately model the tip one needs to know its shape, which is generally not know or only determined *after* the experiment. And even then one should somehow account for screening by the sample and other effects that distort the tip potential, something that is generally not feasible.

When working with semi-conducting 2DEGs, the spot size is generally defined as the depletion zone beneath the tip. This can be obtained experimentally through various ways. One can for example look at interference patterns, created by electrons backscattering on the SGM spot, or look at the bias required to pinch of a quantum point contact [40, 41].

When working with graphene, most of these techniques become inapplicable, due to the bipolar nature of charge carriers in graphene. It is not possible to create a depletion zone, and one cannot completely block transport. Even if a puddle of opposite charge is induced, a certain minimum transport can and will still take place, as the charge carriers can propagate through these puddles, possibly by Klein tunnelling. In fact, close to the charge neutrality point graphene is naturally full of these charge puddles, as a consequence of an inhomogeneous potential and ripples. These charge puddles can be visualised with a SGM [42, 43]. In short, determining the extent of the tip effect on our samples is not trivial.

Detecting backscattering

The electrostatic potential in a region of the graphene determines the local charge carrier density. This in turn influences the local filling factor: a high charge carrier density equals a higher filling factor in the same magnetic field, and visa versa (see section 1.2 on page 4). Thus, we have a handle to influence the edge channels.

For example: we tune the filling factor in the whole device to $\nu = -6$ by applying a negative voltage to the backgate. Then, we move the tip close to

the centre of the ribbon and apply a *positve* voltage to counteract the effect of the backgate. We tune the tip potential such that the gating of the tip is only effective in the centre of the ribbon. This allows us to locally induce filling factor $\nu = -2$, so that we now have a $pp'p$ junction with $p = -6$ and $p' = -2$, as shown in figure 4.4.

Recall from section 1.3 on page 10 that one can only measure backscattering directly if the p' region does not extend to the contacts. If the p' region is well localized at the centre of the ribbon, one can monitor either the diagonal (V_D^+) or longitudinal (V_{xx}) voltage drop. The former reflects the minimum filling factor p' in the centre of the device. The latter —which is normally zero in quantized conditions— will now take a finite value.

In the case of $p = \nu = -6$ and $p' = \nu = -2$, R_{xx} will show a plateau at 8.7 kΩ. To check the filling factor in the p region, one can simply measure the classical Hall voltage V_{xy} on either or on both sides of the device. This voltage drop reflects only the filling factors at the xy-contacts, even if quantum Hall edge channels are backscattered somewhere in the device. See section 1.3 on page 10 for detailed information about the different configurations and the expected influence on the Hall resistances.

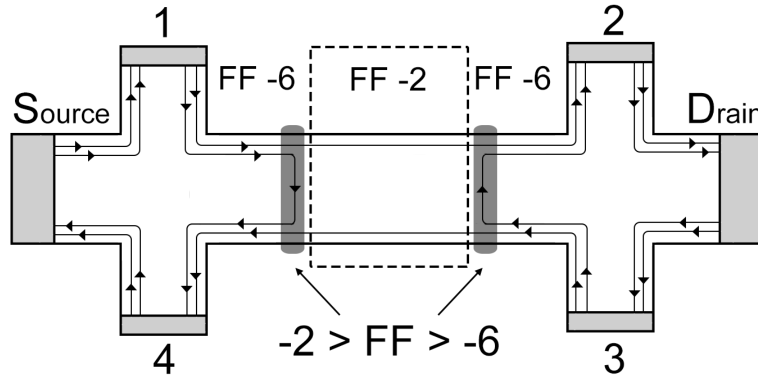

Figure 4.4: A schematic illustration of the quantum Hall effect in a Hall bar. The extra potential induced by the SGM tip is localized in the centre of the device, where it creates a local region of filling factor -2. The edge channels corresponding to the second Landau level cannot enter this region and are forced to backscatter.

To determine the effect of the biased tip, we can monitor R_{xx} and R_{xy} while the tip is at a fixed position, but also while scanning over an area. By scanning with the tip, images are generated which illustrate the effect of the tip at a certain position on R_{xx} and R_{xy}. This allows one to reconstruct how electronic transport is affected and evolves with the tip position.

The unique behaviour of charge carriers in graphene makes it also possible to induce regions of different charge carrier polarity. For example, a *npn*

junction can be created through local electrostatic gating. This however, creates a new effect which is dependent on the equilibration of counter-propagating edge channels, i.e. the p and n type edge channels which meet at the junction between the two regions. This dynamic manifests itself as fractional values of the Hall resistance [27]. These fractional values are dependent on the redistribution of the injected charge carriers over the counter propagating edge channels, while the carriers flow from source to drain. The effect is unrelated to the fractional quantum Hall effect.

This phenomenon is interesting, certainly in combination with the SGM, which grants one a unique control over the junction. It should be straightforward to induce npn junctions with the SGM, using the same approach we used to induce, for example, $pp'p$ junctions. Unfortunately time constraints prohibited any experiments of this nature. Hence, we focused on backscattering channels without creating a bipolar junction, i.e. we avoided inducing regions of different charge carrier polarities.

If the tip is effective in a sufficiently small area, one can reveal the structure of the edge channels —if there is any— by moving the tip towards the ribbon [3, 4]. In the rest of this section we will discuss what would happen *if* reconstruction was taking place, in terms of compressible (C) and incompressible (I) strips.

Let us position the tip far away from the sample, which is at bulk filling factor -6, such that the bulk is insulating and the edge channels do not backscatter to the other edge (see also section 1.2 on page 8). When the tip approaches the sample, it will start to 'feel' the tip potential, and the edge channels on the side closest to the tip will be pushed towards the centre. Once the inner channels are close enough, they will begin to interact and backscatter, causing the conductance to decrease; there is now a compressible (C) strip at the centre [3].

Note that conductance here refers to the total source-drain conductance through the device. This can be determined by measuring the two terminal source-drain voltage, or, to avoid contact resistance, by measuring the diagonal voltage V_D^+. Another possibility is to look at V_{xx} (R_{xx}), which should under these conditions also take non-zero quantized values, as a result of the imbalance in the chemical potential between the left and right side of the device (section 1.3 on page 10). Both R_{xx} and V_D^+ contain the same information. In the measurements presented here we will focus on R_{xx}.

As the tip moves closer, this C strip shrinks until the channels are completely backscattered and the conductance is lowered from $6\frac{e^2}{h}$ to $2\frac{e^2}{h}$. There is now again an incompressible strip at the centre of the ribbon, isolating the remaining edge channels.

Moving the tip even closer will again decrease the width of the I strip, but the conductance will still be quantized. Thus, when the system is in an I state, a plateau will appear in the conductance. The width of this plateau in real space, i.e. the distance you have to move the tip before you leave this

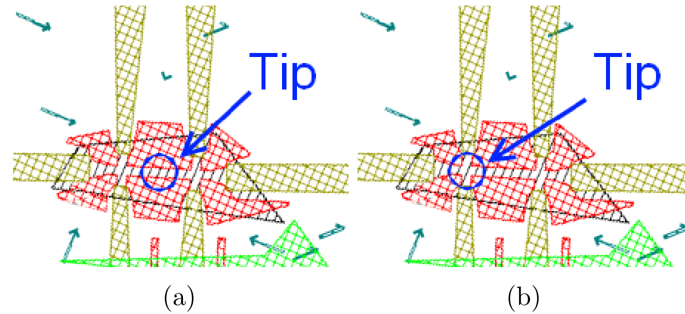

(a) (b)

Figure 4.5: a) The position of the SGM tip at the centre of the graphene ribbon. b) The tip positioned between two Hall contacts. In the experiment the tip was positioned at the *left* side of the device in the AFM scan.

plateau, equals two times the width of the incompressible strip (since there are are two strips; one on each side of the sample). Likewise, the width of the region in between two plateaus where the conductance monotonically decreases, equals twice the width of the compressible region of the edge channels. This way, one can directly probe the edge channel widths and structure, with the SGM.

In this case the precision by which the tip can be positioned with respect to the ribbon determines the resolution, since the channels will try to flow around the region where the tip potential is higher than the energy of the Landau level. Assuming the tip potential size is within the suitable range —comparable to the width of the ribbon, smaller than the length of the ribbon— the actual size of the spot has no influence on the lateral resolution that can be achieved.

SGM measurements

To qualitatively calibrate the effect of the tip we first did several tests while keeping the tip in one fixed position over the centre of the device at zero magnetic field (figure 4.5a). This way one can determine the effect of varying the applied bias and tip-sample distance. Changes in the shape and position of the peak around the Charge Neutrality Point (when sweeping the backgate), illustrate the effect of the tip. If the effective gating area is comparable or larger than the sample, the curve will shift in its entirety, as you are effectively adding another global (back)gate, which works with or against the real backgate, depending on the relative voltages. If the effect is local to only a (significant) part of the device, the CNP will split into two [44].

Figure 4.6 on the following page shows a set of backgate sweeps taken with the tip over the centre of the ribbon. Most notable is the shift of the entire curve, which would imply that the tip effect is rather large compared

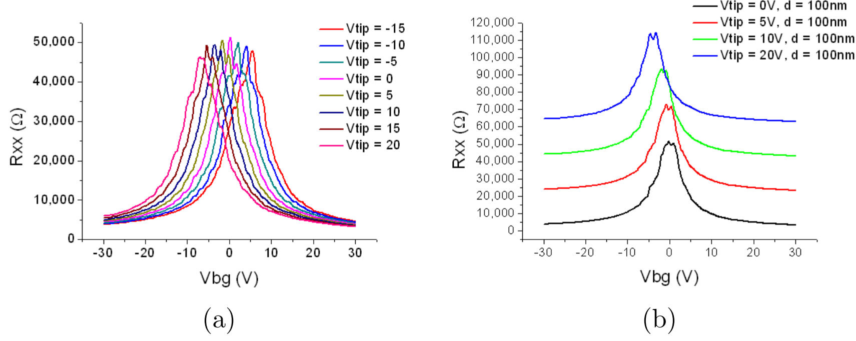

(a) (b)

Figure 4.6: Data collected at $T = 4.2$ K and $B = 0$ T with the SGM tip over the centre of the ribbon. a) The voltage applied to the SGM tip is changed while the distance between the tip and the device is held constant at $d \approx$ 100 nm. A global shift is notable. b) Four curves plotted with an offset for better visibility.

to the 6 µm ribbon. In figure 4.6b, four curves are plotted with an offset for better visibility.

The next logical step is to test the effect of a static tip in a ≈ 8 T magnetic field. Because the Hall contacts are only sensitive to the local filling factor at the contacts (see section 1.3 on page 10 for more details), the tip is now placed in between two contacts (figure 4.5b on the preceding page). By using three different lock-in amplifiers, one for V_{xx}, and one for both combinations of V_{xy} contacts, we can compare the filling factors on the two ends of the graphene ribbon, while applying a potential to one side of the device through the SGM tip.

From figure 4.7 on the next page it is clear that by applying a suitable bias to the tip, we can change the filling factor on one side of the device such that we see the next plateau, while maintaining the original quantization on the other side of the device[2]. While this configuration is convenient to determine the effect of the tip, it does not allow one to directly see any edge channel structure, even if it is clear a channels must be backscattered somewhere in the device.

The two measurements discussed above give us valuable information about the strength and size of the tip potential. When the tip is at the centre of the ribbon, we see a global effect. On the other hand, we clearly see a local effect when the tip is positioned at one side of the device. The first measurement suggest that the area we gate through the tip is at least ≈ 6 µm long, along the length of the ribbon, regardless of the applied bias. The second measurement implies an upper bound for the spot size; ≈ 12 µm

[2]The graphene ribbon is 5 µm long, and the (graphene) leads are ≈ 1 µm wide. Thus the distance between the two centres of the longitudinal contacts is ≈ 6 µm.

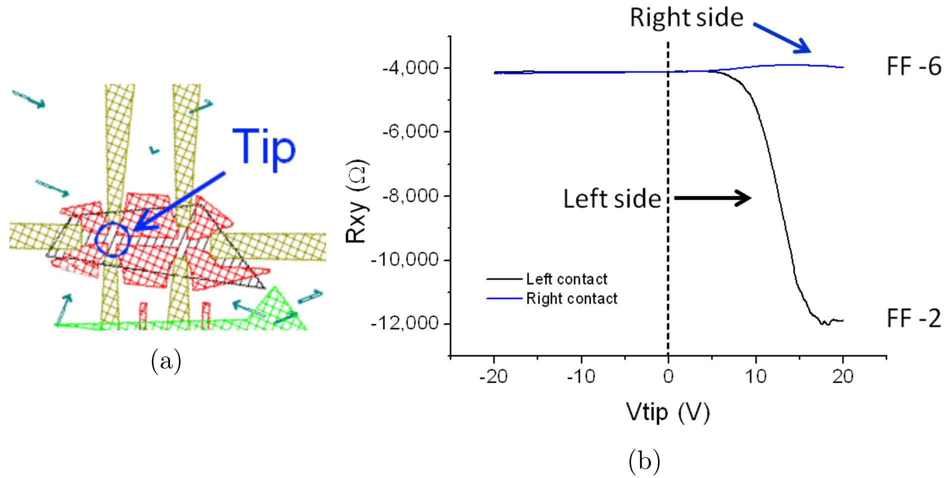

Figure 4.7: a) The tip position b) Data collected at $T = 4.2$ K, $B = 8$ T. This figure shows the effect of the tip, which is stationary between the two Hall contacts on the left side of the device. The backgate is tuned (to the hole side) such that the Hall resistance is quantized at filing factor -6 when no bias is applied to the tip. This corresponds to 6 edge channels or a resistance of $R_{xy} \approx -4.3$ kΩ. By applying a voltage to the SGM tip, the filling factor on the left side is changed to $\nu = -2$ (-12.9 kΩ), while the filling factor on the right hand side remains unchanged. With the tip close to the sample, we generally saw small variations in the resistance of the plateaus.

in the direction of the ribbon. The effect cannot be larger than twice the ribbon's length (12 µm) for if it was, we would also see a global effect with the tip located at the side of the ribbon.

A backgate sweep of R_{xx} with the tip active between the contacts on the left hand side clearly shows splitting (figure 4.8b on the following page). The typical R_{xx} curve is split in two and every peak now appears twice.

Note that the peaks of the two sets have roughly the same height. One would expect this if the potential in roughly half the device is changed. The device can now be seen as a series of two devices, more or less of the same length, while the difference in potential shifts one of the two curves with respect to the backgate potential. Even though R_{xx} is now inhomogeneous (when considering the entire device) the peaks still appear sharp, which indicates that also the potential induced by the tip is relatively sharp. If the tip potential was very shallow, the filling factor in the device would slowly vary along its length, and the peaks in R_{xx} would be washed out.

We denote the two R_{xx} curves which combine to make the total longitudinal resistance (one corresponding to each half of the device) A and B. If an integer but different filling factor is induced in both sides of the device, for example $\nu = -6$ and $\nu = -2$, the central peak of e.g. B2 would align

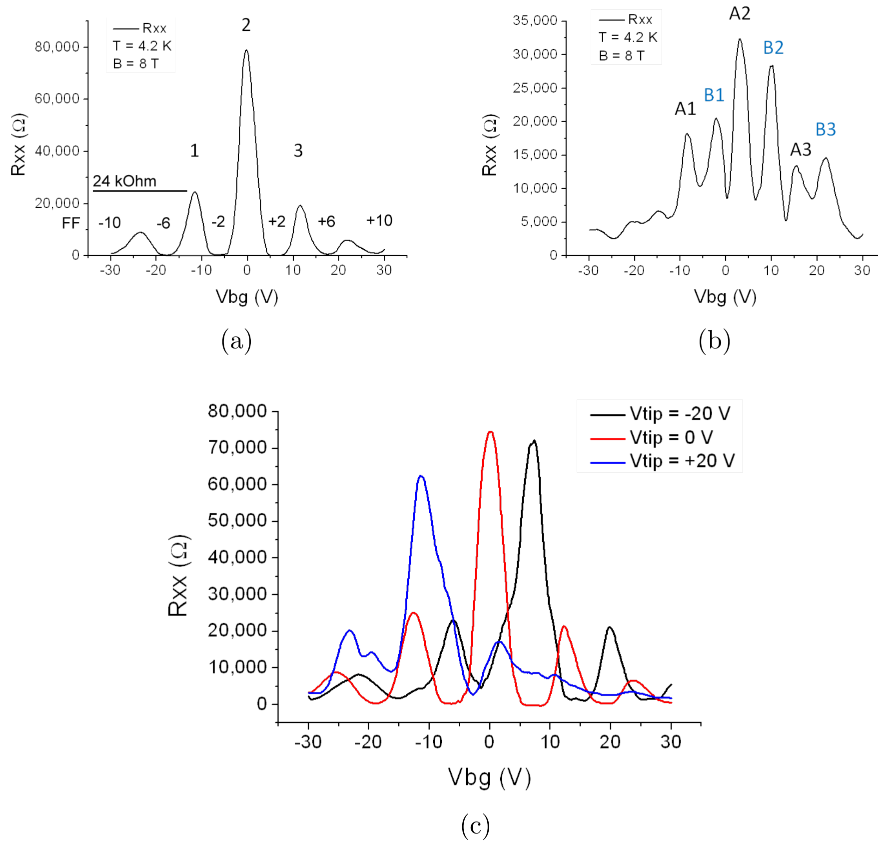

Figure 4.8: Data collected at $T = 4.2$ K and $B = 8$ T. a) A reference curve of R_{xx} taken without the tip. b) When the tip is positioned between the two contacts on the left side of the device, the R_{xx} resistance splits into two; the two sets are denoted A and B. Note that the maximum values of the peaks are almost half the value of those those in the reference curve. c) R_{xx} while the tip is positioned at the centre of the ribbon, with a tip bias of 0, -20 and +20 Volt. A noticeable global shift occurs. Although the shape of the curve is broadened by the presence of the tip, the splitting as seen in b) is largely absent.

with the peak A1. Then, the regions in between the peaks, where R_{xx} is zero, overlap and the total R_{xx} is also zero.

The tip is then placed at the centre of the device, and the measurement is repeated, see figure 4.8c on the previous page. A global shift is seen, comparable to the other measurements where the tip was placed at the centre of the device. There is no clear splitting visible, although the peaks in R_{xx} have become broader and less regular.

These results are consistent with those discussed above: when the tip is at the centre, the effect seems to encompass the entire device, and only a global shift is visible. When the tip is placed between the contacts at the side of the ribbon, a local effect is clearly observable. Combining the aforementioned results, we can conclude that the tip potential is effective in an area of $\approx 7 - 12$ µm long, in the direction of the ribbon.

Having now a rough understanding of the size and magnitude of the gating effect of the tip, we start scanning with the SGM while measuring R_{xx} and R_{xy} on both sides of the device. This gives us images that reflect the tip effect on these transport quantities with the tip at certain positions. By changing the applied tip bias in between scans, we assemble a series of images that show how the effects evolve. Since the effect of the tip appears to be rather large, we choose a long scan range of 1×15 µm^2, perpendicular to the ribbon (figure 4.9 on the following page).

We have selected this range such that the tip has no effect when it is far from the ribbon. So we are sure that the measuring conditions with the tip absent (far away) are identical over all separate scans. With the tip far away, we tune the backgate to the filling factor $\nu = -6$, and $R_{xx} = 0$. We can confirm that the tip has no effect at the end of the scans, by looking at the line profiles in figure 4.10 on page 45. As the tip is far from the ribbon at the top of the scans, all R_{xx} curves converge to 0 resistance.

In the data set presented here we aim to backscatter the channels belonging to the second Landau level, by inducing a local region in the centre of the ribbon where only the first Landau level is filled. Since the second Landau level is fourfold degenerate, while the first Landau level is twofold degenerate, this means we backscatter 4 of the 6 edge channels.

This data is representative of similar sets of data: we also performed experiments backscattering channels at the electron side by creating a local region with filling factor $\nu = +2$ in a ribbon with filling factor $\nu = +6$. Moreover we repeated these backscattering experiments for the third Landau level, i.e. with a global filling factor $\nu = \pm 10$ and a local filling factor $\nu = \pm 6$. All these measurements show good agreement with those presented here.

The SGM scans of R_{xx} (figure 4.10 on page 45) show no plateaus. For a tip bias of 0 or 3 Volt, R_{xx} increases monotonically as the tip approaches the graphene ribbon, and reaches its maximum value when the tip is above the ribbon, before decreasing again as the tip moves on. When a larger tip bias is applied, the resistance reaches a maximum value of around 22 to 24 kΩ

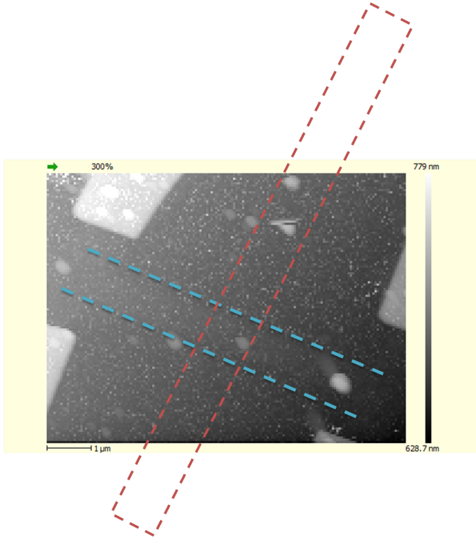

Figure 4.9: An AFM picture illustrating the SGM scan range used. The four side contacts are visible in white. The position of the ribbon is roughly given by the blue lines, and the red dashed lines indicate the scan range, which is 1×15 μm^2 and perpendicular to the ribbon. Some 'dirt' can be seen as white spots around and on the device. Note that the ribbon is not positioned at the centre of the scan range, which is asymmetric with respect to the ribbon.

before it starts to decrease, until the tip passes over the ribbon and the curve is traced back as the tip effect wanes.

As discussed in section 4.2 on page 36 and section 1.3 on page 10, R_{xx} should take a quantized value when a set of edge channels is backscattered. When backscattering four channels, by inducing local region with filling factor -2 in a device with global filling factor -6, R_{xx} should become 8.7 kΩ.

The absence of any plateau suggest that we are unable to induce local backscattering due to the size of the potential induced by the tip. Instead, it appears that there is only a global potential, which changes the filling factor in the entire device. To confirm this, we compare the line profiles presented here, with the reference backgate sweep of R_{xx}, where there is no tip close to the sample (figure 4.8a on page 42). The hight of the peak in R_{xx} between filling factors -6 and -2 is ≈ 24 kΩ. This value is reached in the line scans, which implies that at this point, the bulk of the ribbon becomes resitive along the entire length of the device.

In figure 4.11 on page 46 the corresponding scans of R_{xy} are shown. In the ideal case, these should maintain their original quantization (in this case $\nu = -6$) at all times. However, this is clearly not the case, as the filling factor in between the contacts deviates from -6 when 6 or more Volts are applied to the tip.

The measurement clearly shows that if 12 or more Volts are applied, the regions in between the xy-contacts reach filling factor -2. This again indicates that the effect of the SGM tip extends all the way to the sides of the ribbon.

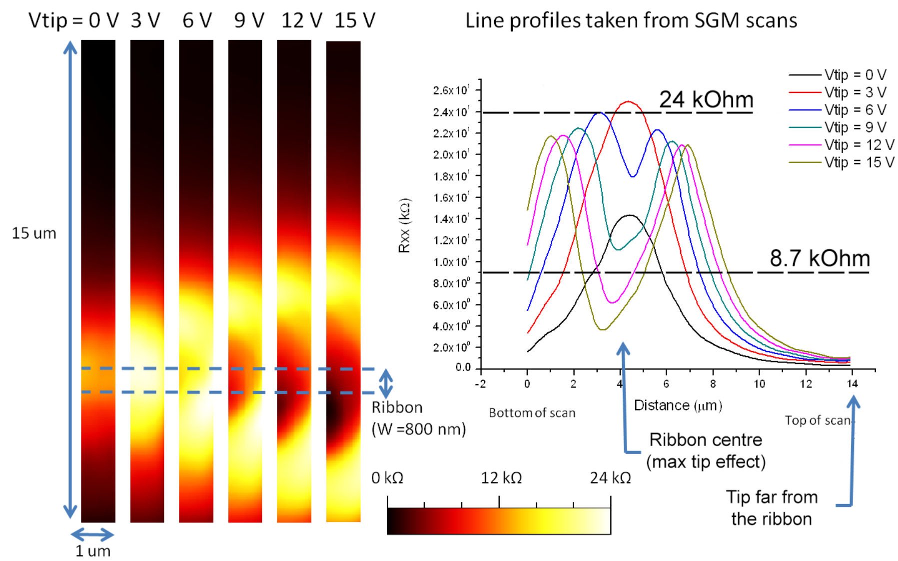

Figure 4.10: A series of SGM scans. From left to right, the same area is scanned while applying a different voltage to the tip. Black equals a small (zero) R_{xx} and a yellow/white colour indicates a high resistance. The position of the ribbon is roughly indicated by the blue dashed line. When the tip is far from the ribbon, at the top of the scan range, the whole ribbon is at filling factor -6, and R_{xx} tends to zero. The plot on the right shows the line profiles, taken along the centre of each scan, from bottom to top. Note that the maximum resistance of ≈ 24 kΩ corresponds to the maximum resistance in R_{xx} when the sample is in between filling factors -6 and -2, without the tip close to the device. See figure 4.8a on page 42.

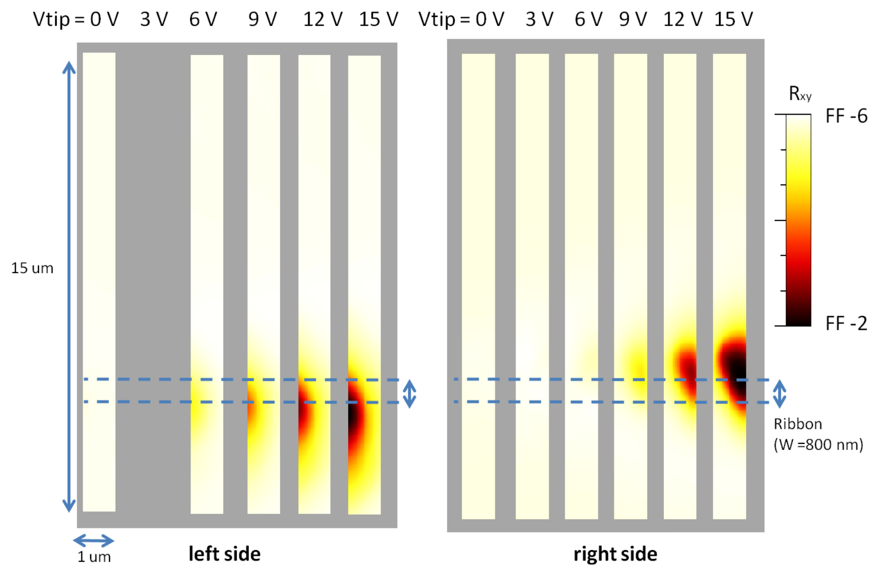

Figure 4.11: The same series as figure 4.10 on the previous page; all three scans (R_{xx} (4.10), R_{xy} at the left side, and R_{xy} at the right side of the device) are taken simultaneously. The Hall resistance on both sides of the device is shown. White/light yellow corresponds to a Hall resistance of -4.3 kΩ, or filling factor -6. In the black area's this resistance equals -12.9 kΩ, or filling factor -2. The first small deviations from quantization at $\nu = -6$ at the sides are seen when 6 Volt is applied to the tip. At higher tip voltages a transition to filling factor -2 is observed. There is some asymmetry between the effect of the tip on the left and right side.

4.3 Discussion

During the experiment the effect of the tip appeared to be different from what we expected; as the effect was consistently weak in a rather large area. After the experiment was finished, we dismounted the SGM tip to inspect it with a scanning electron microscope. From the pictures in figure 4.12 on the following page one can immediately see that the tip was defective. Most probably, the tip crashed into the sample surface while approaching the sample after the cool-down to 4.2 K. After the cooldown, the AFM briefly lost resolution (while the resolution was good at room temperature, before cooldown), before becoming of good quality again. Most likely, the tip picked up some matter from the sample surface, presumably SiO_2, which after some reconstructing functioned as a new AFM tip and provided a good AFM resolution.

The tip is severely bent and has been twisted into itself, as can be seen in figure 4.12 on the next page. The end of the tungsten tip is now a big, relatively flat and elongated area. From the calibration of the SEM the size of the 'tip' can be estimated to be approximately 5 µm on the short side and nearly three times longer on the long side, although the curvature of the tip in the long direction should decrease the induced potential at the extremities of the tip. The matter which is attached to the end and presumably functioned as the new AFM tip is more than 500 nm high.

These micrographs confirmed our suspicions that the tip was not working properly, and the tip shape agrees well with the observed tip effect, if the tip was oriented more or less perpendicular to the ribbon. Not only was the real distance between the conducting tungsten and the device much larger than expected —$d \approx 600$ nm instead of $d < 100$ nm— but also the area of the tip itself was comparable to the 6 µm long ribbon.

This explains why we were only able to measure a convincingly local effect between the longitudinal contacts when the tip was positioned at one side of the sample, while we saw no or only a weak local effect when the tip was placed at the centre of the ribbon, see figure 4.8c on page 42 and figure 4.6 on page 40. This also agrees with the SGM scans (figure 4.10 on page 45), in which we see the line profiles of R_{xx} at different tip voltages converge only when the distance between the tip and the ribbon becomes $d > 8$ µm.

The height of the material attached to the tip —at least 500 nm— also explained why we saw no to little change when changing the tip sample distance between 30 and 150 nm (figures not shown here).

The last remaining question is now whether our SGM scans contain some information regarding the structure of the edge channels. To directly measure the backscattering of edge channels, and therefore to see the structure of these edge channels, requires the backscattering to be well localized in between the contacts. If the central region with the lower filling factor extends to one or

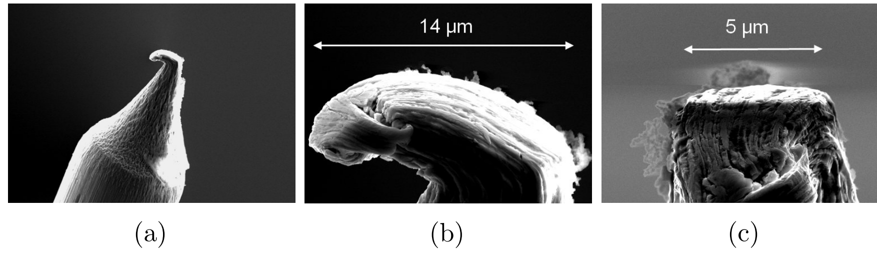

(a) (b) (c)

Figure 4.12: a) A scanning electron microscopy image of the tip used, after the experiment. The tip is obviously deformed. The wire from which the tip is etched has a diameter of 50 µm. b) The same tip shown from the side. Some material, presumably SiO_2, is attached to the tip. c) A close up of the tip rotated by 90 degrees. The tip appears flat and is approximately 6 µm wide. The extra material seems roughly 500 nm high.

both of the side contacts, it is no longer possible to probe the edge channel structure (section 1.3 on page 10). Thus, the large tip and by extension, the large tip potential could be problematic.

The occurrence of plateaus in R_{xx} hinges on two important conditions. First the device must be in state such that transport can only occur through the edge channels. The bulk can only be conductive in some localized region in the ribbon, and therefore allows backscattering between the opposing edges in this region, but it should not add a separate contribution to the overall conductivity. To fulfil this condition, a sharp tip potential is required, which would induce a sharp transition between the regions of different filling factor.

Secondly, it is necessary that the region where the quantization differs from the global quantization induced by the backgate is well localized in between the contacts. If this is not the case, one cannot probe the structure of the edge channels, even if they are backscattered somewhere in the device. This demand can be seen as a stronger version of the first condition as it states that the filling factor must be well quantized at both ends of the ribbon.

Finally, if electrostatic reconstruction takes place, the width of the plateaus in R_{xx} would correspond to the width of the incompressible stripes, and the transition region in between the plateaus corresponds to the width of the compressible strips.

If the first condition does not hold (the bulk is conductive along the device), the situation becomes significantly more complex, as one needs to find a way to subtract the unwanted contribution of the bulk conductance, which might obscure the sought features. Furthermore, the second requirement would also be violated. As a consequence one would no longer be sensitive to the edge channel structure.

If no reconstruction takes place, one would still expect plateaus in R_{xx} as the edge channels are backscattered one by one. However there would be very sharp transitions between the different plateaus, as the compressible regions would in this case very small to non existing, and the edge channels would behave as monolithic objects.

It is trivial to note that in SGM scans of R_{xx} no plateau appear at the theoretical value of 8.7 kΩ, nor at any other value. In fact, these SGM scans effectively map out the R_{xx} curve taken without the tip close to the sample, as the maximum resistance approaches the same value. This implies that when the tip is over the centre of the ribbon, it has a global gating effect which leads to a conducting bulk over the entire length of the ribbon.

This agrees with the scans of R_{xy}, which lose their exact quantization —and in fact soon after reach the next plateau— already at a moderate tip bias, while the tip is several micrometers from the corresponding contacts.

It is thus our conclusion that the gating effect of the tip, which was comparable to the length of our device, was too large (in terms of affected area) to reveal the structure of the edge channels.

Chapter 5

Conclusions

In this final chapter, a brief summary of the work presented here is given. Hereafter some concluding remarks are given and a possible continuation of this work is briefly discussed.

The goal of this work was to investigate and manipulate edge channel transport in the quantum Hall regime through Scanning Gate Microscopy. To perform this experiment one not only needs a sensitive SGM set up, which allows transport measurements at low temperatures (down to 300 mK) and moderately high magnetic fields (up to 8 Tesla), but also devices which adhere to rather strict conditions. In the case of this thesis, graphene devices with a high mobility were required, as the target experiment requires a well defined quantum Hall effect. Furthermore, the device geometry has to be carefully chosen and matched with the dimensions of the optimum tip potential. Thus, the width of these devices should not be too large nor too small, while retaining an adequate length and good performance.

Multiple graphene nanoribbon FETs were designed and produced to facilitate this challenging experiment, based on experience and the characterization of these devices through low temperature magneto-transport. These devices were produced in the cleanroom at the NEST laboratory and characterized by low temperature magneto-transport measurements.

Ultimately, a largely successful SGM measurement was performed. We were able to find and even see the graphene nanoribbon device through AFM, and observed a well defined quantum Hall effect in our devices. Moreover, we have incontestably shown that we can control the filling factor on one side of our nanoribbon device, while the original quantization is maintained on the other side, ≈ 6 μm far away. This demonstrates the general feasibility of our ideas and shows that we can achieve a local control of the quantum Hall edge channels through SGM, even though the field effect of the SGM tip turned out much larger than intended.

Concluding remarks

Regrettably, we did not succeed in reaching our more ambitious goal of revealing the the edge channel structure, due to a mechanical failure of our SGM tip. The deformation of the tungsten tip greatly extended the area effected by the tip potential, such that is was comparable with the length of our device, while reducing the strength and probably the sharpness of this potential. Hence, we are not yet able to answer the question of the edge channel reconstruction, as it requires local gating with a precision that was not obtained in this experimental run. However, I am confident that this final touch would be straightforward with a new tip, now that we have demonstrated that all other requirements are adhered to.

The daily life in experimental physics is particularly rich. It is filled to the brim with challenges, failures, discoveries, disappointments, many promising devices, more broken devices and a lot of hard work. There is of course also the occasional success, which makes the whole journey worthwhile. I assume that my experience at NEST, with all its struggles and charms, was no exceptional case.

Nevertheless it feels particularly unsatisfying to —after having overcome so many challenges— fall short due to something so small as a deformed SGM tip. Unfortunately a typical lack of time did not allow me to attempt another try.

Assuming an opportunity will present itself later this year, I would be more than happy to take one more stab at this beautiful experiment, which has been the focus of my past year. The plan is simple for a change: all I would need is a good tip!

Bibliography

[1] K. S. Novoselov, A. K. Geim, S. V. Morozov, D. Jiang, Y. Zhang, S. V. Dubonos, I. V. Grigorieva, and A. A. Firsov, "Electric Field Effect in Atomically Thin Carbon Films," *Science*, vol. 306, pp. 666–669, 2004.

[2] A. C. Ferrari, F. Bonaccorso, V. Falko, K. S. Novoselov, S. Roche, P. Bøggild, S. Borini, F. Koppens, V. Palermo, N. Pugno, J. A. Garrido, R. Sordan, A. Bianco, L. Ballerini, M. Prato, E. Lidorikis, J. Kivioja, C. Marinelli, T. Ryhänen, A. Morpurgo, J. N. Coleman, V. Nicolosi, L. Colombo, A. Fert, M. Garcia-Hernandez, A. Bachtold, G. F. Schneider, F. Guinea, C. Dekker, M. Barbone, C. Galiotis, A. Grigorenko, G. Konstantatos, A. Kis, M. Katsnelson, C. W. J. Beenakker, L. Vandersypen, A. Loiseau, V. Morandi, D. Neumaier, E. Treossi, V. Pellegrini, M. Polini, A. Tredicucci, G. M. Williams, B. H. Hong, J. H. Ahn, J. M. Kim, H. Zirath, B. J. van Wees, H. van der Zant, L. Occhipinti, A. Di Matteo, I. a. Kinloch, T. Seyller, E. Quesnel, X. Feng, K. Teo, N. Rupesinghe, P. Hakonen, S. R. T. Neil, Q. Tannock, T. Löfwander, and J. Kinaret, "Science and technology roadmap for graphene, related two-dimensional crystals, and hybrid systems," *Nanoscale*, vol. 7, pp. 4598–4810, 2014.

[3] N. Paradiso, S. Heun, S. Roddaro, L. N. Pfeiffer, K. W. West, L. Sorba, G. Biasiol, and F. Beltram, "Selective control of edge-channel trajectories by scanning gate microscopy," *Phys. E Low-Dimensional Syst. Nanostructures*, vol. 42, pp. 1038–1041, 2010.

[4] N. Paradiso, S. Heun, S. Roddaro, L. Sorba, F. Beltram, G. Biasiol, L. N. Pfeiffer, and K. W. West, "Imaging fractional incompressible stripes in integer quantum hall systems," *Phys. Rev. Lett.*, vol. 108, pp. 1–5, 2012.

[5] N. Paradiso, S. Heun, S. Roddaro, G. Biasiol, L. Sorba, D. Venturelli, F. Taddei, V. Giovannetti, and F. Beltram, "Imaging backscattering through impurity-induced antidots in quantum Hall constrictions," *Phys. Rev. B - Condens. Matter Mater. Phys.*, vol. 86, pp. 1–6, 2012.

[6] S. D. Sarma, M. Freedman, and C. Nayak, "Topologically protected qubits from a possible non-abelian fractional quantum hall state," *Phys. Rev. Lett.*, vol. 94, pp. 1–4, 2005.

[7] G. Moore and N. Read, "Nonabelions in the fractional quantum hall effect," *Nucl. Phys. B*, vol. 360, pp. 362–396, 1991.

[8] C. Nayak, S. H. Simon, A. Stern, M. Freedman, and S. Das Sarma, "Non-Abelian anyons and topological quantum computation," *Rev. Mod. Phys.*, vol. 80, pp. 1083–1159, 2008.

[9] A. Chang, L. Pfeiffer, and K. West, "Observation of Chiral Luttinger Behavior in Electron Tunneling into Fractional Quantum Hall Edges," *Phys. Rev. Lett.*, vol. 77, pp. 2538–2541, 1996.

[10] M. Grayson, D. C. Tsui, L. N. Pfeiffer, K. W. West, and A. M. Chang, "Continuum of Chiral Luttinger Liquids at the Fractional Quantum Hall Edge," *Phys. Rev. Lett.*, vol. 80, pp. 1062–1065, 1998.

[11] A. H. Castro Neto, F. Guinea, N. M. R. Peres, K. S. Novoselov, and A. K. Geim, "The electronic properties of graphene," *Rev. Mod. Phys.*, vol. 81, pp. 109–162, 2009.

[12] S. D. Sarma, S. Adam, E. H. Hwang, and E. Rossi, "Electronic transport in two dimensional graphene," *Rev. Mod. Phys.*, vol. 83, pp. 1–85, 2011.

[13] P. R. Wallace, "The band theory of graphite," *Phys. Rev.*, vol. 71, pp. 622–634, 1947.

[14] N. D. Mermin, "Crystalline order in two dimensions," *Phys. Rev.*, vol. 176, pp. 250–254, 1968.

[15] M. Y. Han, Y. Zhang, and P. Kim, "Energy band-gap engineering of graphene nanoribbons," *Phys. Rev. Lett.*, vol. 98, pp. 1–4, 2007.

[16] F. Duerr, J. B. Oostinga, C. Gould, and L. W. Molenkamp, "Edge state transport through disordered graphene nanoribbons in the quantum Hall regime," *Phys. Rev. B - Condens. Matter Mater. Phys.*, vol. 86, pp. 2–5, 2012.

[17] R. B. Laughlin, "Quantized Hall conductivity in two dimensions," *Phys. Rev. B*, vol. 23, pp. 5632–5633, 1981.

[18] M. Büttiker, "Absence of backscattering in the quantum Hall effect in multiprobe conductors," *Phys. Rev. B*, vol. 38, pp. 9375–9389, 1988.

[19] K. S. Novoselov, Z. Jiang, Y. Zhang, S. V. Morozov, H. L. Stormer, U. Zeitler, J. C. Maan, G. S. Boebinger, P. Kim, and A. K. Geim, "Room-Temperature Quantum Hall Effect in Graphene," *Science).*, vol. 315, pp. 1379–1379, 2007.

[20] A. J. M. Giesbers, U. Zeitler, M. I. Katsnelson, L. A. Ponomarenko, T. M. Mohiuddin, and J. C. Maan, "Quantum-hall activation gaps in graphene," *Phys. Rev. Lett.*, vol. 99, pp. 1–4, 2007.

[21] D. B. Chklovskii, B. I. Shklovskii, and L. I. Glazman, "Electrostatics of edge channels," *Phys. Rev. B*, vol. 46, pp. 4026–4034, 1992.

[22] D. B. Chklovskii, K. A. Matveev, and B. I. Shklovskii, "Ballistic conductance of interacting electrons in the quantum Hall regime," *Phys. Rev. B*, vol. 47, no. 19, pp. 12605–12617, 1993.

[23] B. W. Alphenaar, P. L. McEuen, R. G. Wheeler, and R. N. Sacks, "Selective equilibration among the current-carrying states in the quantum hall regime," *Phys. Rev. Lett.*, vol. 64, pp. 677–680, 1990.

[24] C. Chamon and X.-G. Wen, "Sharp and smooth edge of quantum Hall states," *Phys. Rev. B*, vol. 49, p. 8227, 1994.

[25] P. G. Silvestrov and K. B. Efetov, "Charge accumulation at the boundaries of a graphene strip induced by a gate voltage: Electrostatic approach," *Phys. Rev. B - Condens. Matter Mater. Phys.*, vol. 77, pp. 1–5, 2008.

[26] J. R. Williams, L. Dicarlo, and C. M. Marcus, "Quantum Hall Effect in a," *Science (80-.).*, vol. 1, no. August, pp. 1–4, 2007.

[27] D. a. Abanin and L. S. Levitov, "Quantized Transport in Graphene p-n Junctions in a Magnetic Field.," *Science*, vol. 317, pp. 641–643, 2007.

[28] J. V. Velasco, G. Liu, W. Bao, and C. N. Lau, "Electrical transport in high-quality graphene pnp junctions," *New J. Phys.*, vol. 11, 2009.

[29] P. Blake, E. W. Hill, A. H. Castro Neto, K. S. Novoselov, D. Jiang, R. Yang, T. J. Booth, and A. K. Geim, "Making graphene visible," *Appl. Phys. Lett.*, vol. 91, 2007.

[30] A. C. Ferrari, J. C. Meyer, V. Scardaci, C. Casiraghi, M. Lazzeri, F. Mauri, S. Piscanec, D. Jiang, K. S. Novoselov, S. Roth, and A. K. Geim, "Raman spectrum of graphene and graphene layers," *Phys. Rev. Lett.*, vol. 97, pp. 1–4, 2006.

[31] V. Miseikis, D. Convertino, N. Mishra, M. Gemmi, T. Mashoff, S. Heun, N. Haghighian, F. Bisio, M. Canepa, V. Piazza, and C. Coletti, "Rapid CVD growth of millimetre-sized single crystal graphene using a cold-wall reactor," *2D Mater.*, vol. 2, no. 1, p. 014006, 2015.

[32] S. Xiang, V. Miseikis, L. Planat, S. Guiducci, S. Roddaro, C. Coletti, and F. Beltram, "Low-temperature quantum transport in CVD-grown single crystal graphene," *Nano Res.*, vol. 014006, p. 146805, 2015.

[33] Y. Wang, Y. Zheng, X. Xu, E. Dubuisson, Q. Bao, J. Lu, and K. P. Loh, "Electrochemical delamination of CVD-grown graphene film: Toward the recyclable use of copper catalyst," *ACS Nano*, vol. 5, pp. 9927–9933, 2011.

[34] B. Huard, N. Stander, J. A. Sulpizio, and D. Goldhaber-Gordon, "Evidence of the role of contacts on the observed electron-hole asymmetry in graphene," *Phys. Rev. B - Condens. Matter Mater. Phys.*, vol. 78, pp. 1–4, 2008.

[35] M. Evaldsson, I. V. Zozoulenko, H. Xu, and T. Heinzel, "Edge-disorder-induced Anderson localization and conduction gap in graphene nanoribbons," *Phys. Rev. B - Condens. Matter Mater. Phys.*, vol. 78, pp. 1–4, 2008.

[36] P. A. Lee and A. D. Stone, "Universal conductance fluctuations in metals," *Phys. Rev. Lett.*, vol. 55, pp. 1622–1625, 1985.

[37] P. A. Lee, "Universal conductance fluctuations in metals: Effects of finite temperature, interactions, and magnetic field," *Phys. Rev. B*, vol. 35, pp. 1039–1070, 1987.

[38] A. Mreńca-Kolasińska, S. Heun, and B. Szafran, "Aharonov-Bohm interferometer based on n-p junction in graphene nanoribbons," *Phys. Rev. B*, vol. 125411, pp. 1–8, 2016.

[39] B. Szafran, "Scanning gate microscopy simulations for quantum rings: Effective potential of the tip and conductance maps," *Phys. Rev. B - Condens. Matter Mater. Phys.*, vol. 84, no. 7, pp. 1–14, 2011.

[40] P. Liu, F. Martins, B. Hackens, L. Desplanque, X. Wallart, M. G. Pala, S. Huant, V. Bayot, and H. Sellier, "Formation of quantum dots in the potential fluctuations of InGaAs heterostructures probed by scanning gate microscopy," *Phys. Rev. B - Condens. Matter Mater. Phys.*, vol. 91, no. 7, pp. 1–13, 2015.

[41] R. Steinacher, A. A. Kozikov, C. Rössler, C. Reichl, W. Wegscheider, T. Ihn, and K. Ensslin, "Scanning-gate-induced effects and spatial mapping of a cavity," *New J. Phys.*, vol. 17, p. 43043, 2015.

[42] R. Jalilian, L. a. Jauregui, G. Lopez, J. Tian, C. Roecker, M. M. Yazdanpanah, R. W. Cohn, I. Jovanovic, and Y. P. Chen, "Scanning gate microscopy on graphene: charge inhomogeneity and extrinsic doping.," *Nanotechnology*, vol. 22, p. 295705, 2011.

[43] M. R. Connolly, K. L. Chiou, C. G. Smith, D. Anderson, G. A. C. Jones, A. Lombardo, A. Fasoli, and A. C. Ferrari, "Scanning gate microscopy

of current-annealed single layer graphene," *Appl. Phys. Lett.*, vol. 96, pp. 9–12, 2010.

[44] F. Amet, J. R. Williams, K. Watanabe, T. Taniguchi, and D. Goldhaber-Gordon, "Insulating behavior at the neutrality point in single-layer graphene," *Phys. Rev. Lett.*, vol. 110, pp. 1–5, 2013.

Acknowledgements

First and foremost, I would like to thank Stefan Heun, for supervising me on a daily basis. I am very grateful for all his advice, answers, help and encouragement, which has culminated in the successful completion of this master thesis.

I would also like to thank my colleagues at NEST, in particular Shaohua Xiang and Stefano Guiducci, with whom I worked in close collaboration and who have helped and guided me on numerous occasions. Moreover I would like to thank Alina Mreńca-Kolasińska, for her stimulating questions and discussions. My gratitude extends to all other people at NEST, who have made my stay in Pisa a pleasant one.

Finally, I would like to thank Jan-Kees Maan, who first suggested this project, who has been my supervisor in the Netherlands, and who has advised me on multiple occasions, for which I am grateful.